# Chapter 1

# Spontaneous pattern formation in primary visual cortex

*Paul C. Bressloff*[1] *and Jack D. Cowan*[2]
[1]*Department of Mathematics, University of Utah, Salt Lake City, Utah 84112*
[2]*Mathematics Department, University of Chicago, Chicago Il. 60637*

## 1.1   Introduction

The primary visual cortex (V1) is the first cortical area to receive visual information transmitted by ganglion cells of the retina via the lateral geniculate nucleus (LGN) of the thalmus to the back of the brain (see figure 1.1). A fundamental property of the functional architecture of V1 is an orderly retinotopic mapping of the visual field onto the surface of cortex, with the left and right halves of visual field mapped onto the right and left cortices respectively. Except close to the fovea (centre of the visual field), this map can be approximated by the complex logarithm (see figure 1.2). Let $\mathbf{r}_R = \{r_R, \theta_R\}$ be a point in the visual field represented in polar coordinates and let $\mathbf{r} = \{x, y\}$ be the corresponding point in the cortex given in Cartesian coordinates. Under the retino-cortical map, $\mathbf{r} = \{\log \mathbf{r}_R, \theta_R\}$. Evidently, if we introduce the complex representation of $\mathbf{r}_R$, $z_R = \mathbf{r}_R \mathrm{e}^{i\theta_R}$ then $z = \log z_R = \log r_R + i\theta_R = x + iy$ generates the complex cortical representation. One of the interesting properties of the retino-cortical map is that the action of rotations and dilatations in the visual field correspond to translations in the $x$ and $y$ directions, respectively, in cortex.

Superimposed upon the retinotopic map are a number of additional feature maps reflecting the fact that neurons respond preferentially to stimuli with particular features [38, 43, 55]. For example, most cortical cells signal the local *orientation* of a contrast edge or bar—they are tuned to
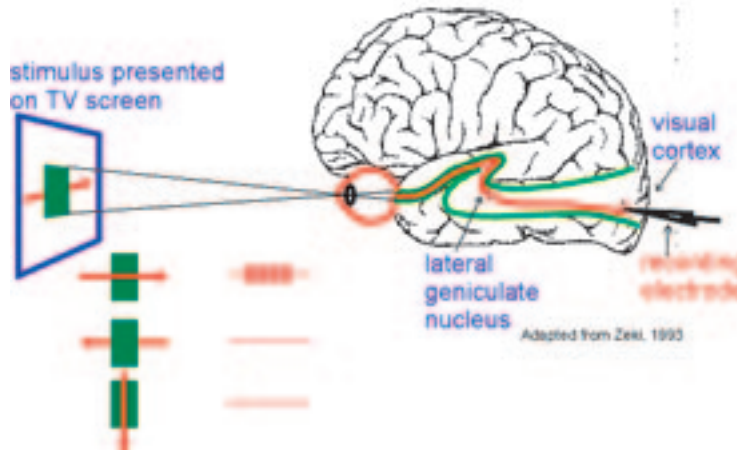
**Figure 1.1.** The visual pathway

a particular local orientation [33]. Cells also show a left/right eye prefer-
ence known as ocular dominance and some are also direction selective. The
latter is illustrated in figure 1.1 where the response of a cell to a moving
bar is shown. In recent years much information has accumulated about
the distribution of orientation selective cells in V1 [27]. In figure 1.3 is
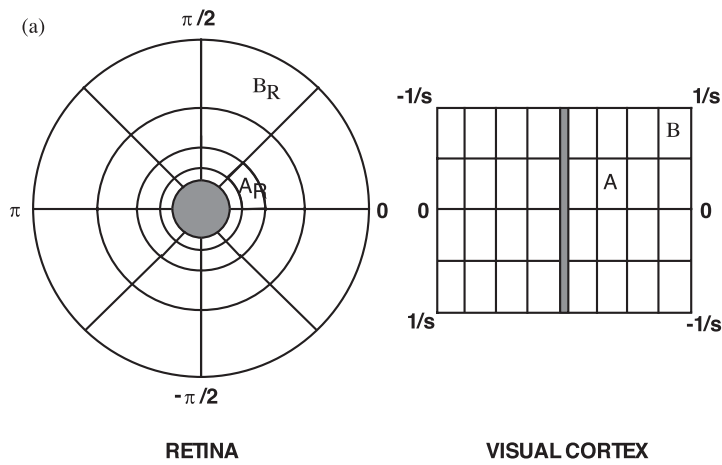given a typical arrangement of such cells, obtained *via* microelectrodes im-



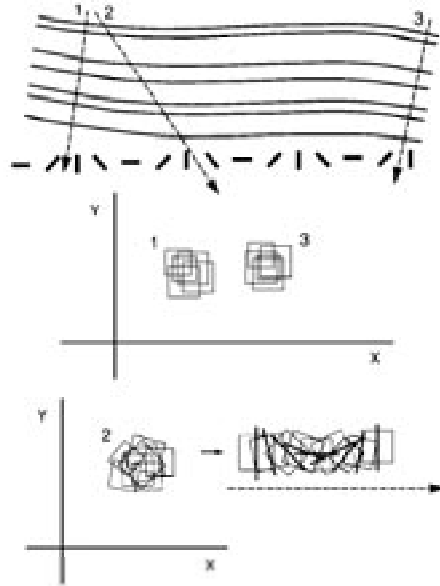**Figure 1.2.** The retino-cortical map generated by the complex logarithm

**Figure 1.3.** Orientation tuned cells in layers of V1 which is shown in cross-section. Note the constancy of orientation preference at each cortical location [electrode tracks 1 and 3], and the rotation of orientation preference as cortical location changes [electrode track 2]. Redrawn from [27].

planted in Cat V1. The first panel shows how orientation preferences rotate smoothly over the surface of V1, so that approximately every $300\mu m$ the same preference reappears, i.e. the distribution is $\pi$–periodic in the orientation preference angle. The second panel shows the receptive fields of the cells, and how they change with V1 location. The third panel shows more clearly the rotation of such fields with translation across V1.

A more complete picture of the two–dimensional distribution[1] of both orientation preference and ocular dominance has been obtained using optical imaging techniques [5, 7, 6]. The basic experimental procedure involves shining light directly on to the surface of the cortex. The degree of light absorption within each patch of cortex depends on the local level of activity. Thus, when an oriented image is presented across a large part of

---

[1] The cortex is of course three-dimensional since it has non-zero thickness with a distinctive layered structure. However, one find that cells with similar feature preferences tend to arrange themselves in vertical columns so that to a first approximation the layered structure of cortex can be ignored. For example, electrode track 1 in figure 1.3 is a vertical penetration of cortex that passes through a single column of cells with the same orientation preference and ocular dominance.

the visual field, the regions of cortex that are particularly sensitive to that stimulus will be differentiated. (An example of optical imaging data is shown in figure 1.5). The basic topography revealed by these methods has a number of characteristic features [43]: (i) Orientation preference changes continuously as a function of cortical location except at singularities (or pinwheels). (ii) There exist linear regions, approximately $800 \times 800\mu m^2$ in area (in macaque monkeys), bounded by singularities, within which iso-orientation regions form parallel slabs. (iii) Iso-orientation slabs tend to cross the borders of ocular dominance stripes at right angles. Singularities tend to align with the centers of ocular dominance stripes. These experimental findings suggest that there is an underlying periodicity in the microstructure of V1 with a period of approximately $1mm$ (in cats and primates). The fundamental domain of this periodic tiling of the cortical plane is the hypercolumn [34, 38], which contains two sets of orientation preferences $\phi \in [0, \pi)$, one for each eye, organized around a set of four singularities (see figure 1.4).



**Figure 1.4.** Iso–orientation contours in a hypercolumn. There are two ocular dominance columns corresponding to left ($L$) and right ($R$) eye preference. Each ocular dominance column contains two orientation singularities or pinwheels. A dashed ring is drawn around one orientation singularity. Redrawn from [6]

Given the existence of a regularly repeating set of orientation and ocular dominance maps, how does such a periodic structure manifest itself anatomically? Two cortical circuits have been fairly well characterized. There is a local circuit operating at sub-hypercolumn dimensions in which cells make connections with most of their neighbors in a roughly isotropic fashion [21]. The other circuit operates between hypercolumns, connecting cells with similar functional properties separated by several millimetres of cortical tissue. Optical imaging combined with labelling techniques has generated considerable information concerning the pattern of connections
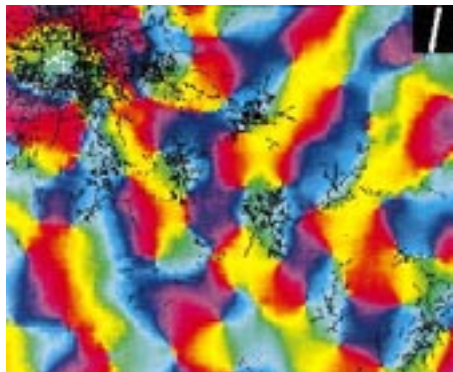
**Figure 1.5.** Lateral Connections made by a cells in Tree Shrew V1. A radioactive tracer is used to show the locations of all terminating axons from cells in a central injection site, superimposed on an orientation map obtained by optical imaging. (Patches with the same coarse-grained orientation preference are shown in the same colour – this is purely for visualization purposes). The patchy distribution of the lateral connections is clearly seen, linking regions of like orientation preference along a particular visuotopic axis. The local axonal field, on the other hand, is isotropic and connects all neurons within a neighbourhood ($\approx 0.7$ mm) of the injection site. Redrawn from [9].

both within and between hypercolumns [5, 6, 40, 66, 9]. A particularly striking result concerns the intrinsic lateral connections of V1. The axons of these connections make terminal arbors only every 0.7 mm or so along their tracks [47, 26], and they seem to connect mainly to cells with similar orientation preferences [40, 66, 9]. In addition, as shown in figure 1.5, there is a pronounced anisotropy of the pattern of such connections: its long axis runs parallel to a patch's preferred orientation [26, 9]. Thus differing iso-orientation patches connect to patches in neighbouring hypercolumns in differing directions. Ongoing studies of feedback connections from points in extrastriate areas back to area V1 [1], show that these connectional fields are also distributed in highly regular geometric patterns, having a topographic spread of up to 13mm that is significantly larger than the spread of intrinsic lateral connections. Stimulation of a hypercolumn via lateral or feedback connections modulates rather than initiates spiking activity [31, 57]. Thus this long-range connectivity is ideally structured to provide local cortical processes with contextual information about the global nature of stimuli. As a consequence the lateral connections have been invoked to explain a wide variety of context-dependent visual processing phenomena

[28, 24, 16].

From the perspective of nonlinear dynamics, there are two very distinct questions one can ask about the large-scale structure of cortex: (i) how did the feature maps and connectivity patterns first develop? (ii) what types of spontaneous and stimulus-driven spatio-temporal dynamics arise in the mature cortex? It appears that in both cases the Turing mechanism for spontaneous pattern formation plays a crucial role.

## 1.2 The Turing mechanism and its role in cooperative cortical dynamics

In 1952 Turing [58] introduced an important set of new ideas concerning spontaneous pattern formation. The details are well known, but we will restate them here by way of providing a context for the rest of this chapter. Turing considered the development of animal coat markings as a problem of pattern formation. He started by introducing the idea that chemical markers in the skin comprise a system of diffusion–coupled chemical reactions among substances called *morphogens*. Turing introduced the following two–component reaction–diffusion system:

$$\frac{\partial \mathbf{c}}{\partial t} = \mathbf{f}(\mathbf{c}) + D\nabla^2 \mathbf{c} \tag{1.1}$$

where $\mathbf{c}$ is a vector of morphogen concentrations, $\mathbf{f}$ is (in general) a nonlinear vector function representing the reaction kinetics and $D$ is the (diagonal) matrix of positive diffusion coefficients. What Turing showed was that there can exist two different reactions such that in the absence of diffusion ($D = 0$), $\mathbf{c}$ tends to a linearly stable homogeneous state, and when $D \neq 0, D_1 \neq D_2$, the homogeneous state becomes unstable and $\mathbf{c}$ tends to a spatially inhomogeneous state. This was the now famous *diffusion driven instability*.

Wilson and Cowan introduced exactly the same mechanism in a neural context [64, 65]. Here we briefly summarize their formulation. Let $a_E(\mathbf{r}, t)$ be the activity of excitatory neurons in a given volume element of a slab of neural tissue located at $\mathbf{r} \in \mathbf{R}^2$, and $a_I(\mathbf{r}, t)$ the correspond activity of inhibitory neurons. $a_E$ and $a_I$ can be interpreted as local spatio–temporal averages of the membrane potentials or voltages of the relevant neural populations. In case neuron activation rates are low they can be shown to satisfy nonlinear evolution equations of the form:

$$\tau \frac{\partial a_E(\mathbf{r}, t)}{\partial t} = -a_E(\mathbf{r}, t) + \tau \int_{\mathbf{R}^2} w_{EE}(\mathbf{r}|\mathbf{r}')\sigma_E[a_E(\mathbf{r}', t)]d\mathbf{r}'$$
$$-\tau \int_{\mathbf{R}^2} w_{EI}(\mathbf{r}|\mathbf{r}')\sigma_I[a_I(\mathbf{r}', t)]d\mathbf{r}' + h_E(\mathbf{r}, t)$$

$$\tau\frac{\partial a_I(\mathbf{r},t)}{\partial t} = -a_I(\mathbf{r},t) + \tau\int_{\mathbf{R}^2} w_{IE}(\mathbf{r}|\mathbf{r}')\sigma_E[a_E(\mathbf{r}',t)]d\mathbf{r}'$$

$$-\tau\int_{\mathbf{R}^2} w_{II}(\mathbf{r}|\mathbf{r}')\sigma_I[a_I(\mathbf{r}',t)]d\mathbf{r}' + h_I(\mathbf{r},t) \qquad (1.2)$$

where $w_{lm}(\mathbf{r}|\mathbf{r}') = w_{lm}(|\mathbf{r}-\mathbf{r}'|)$ gives the weight per unit volume of all synapses to the $l$th population from neurons of the $m$th population a distance $|\mathbf{r}-\mathbf{r}'|$ away, $\sigma_E$ and $\sigma_I$ are taken to be smooth output functions

$$\sigma(x) = \frac{1}{\tau}\frac{1}{1+e^{-\eta(x-\kappa)}} \qquad (1.3)$$

where $\eta$ determines the slope or sensitivity of the input–output characteristics of the population and $\kappa$ is a threshold, $h_E$ and $h_I$ are external stimuli, and $\tau$ is the membrane time constant.

Eqns. (1.2) can be rewritten in the more compact form:

$$\tau\frac{\partial a_l(\mathbf{r},t)}{\partial t} = -a_l(\mathbf{r},t) + \tau\sum_{m=E,I}\int_{\mathbf{R}^2} w_{lm}(|\mathbf{r}-\mathbf{r}'|)\sigma[a_m(\mathbf{r}',t)]d\mathbf{r}'$$

$$+ h_l(\mathbf{r},t) \qquad (1.4)$$

Note that $w_{lE} \geq 0$ and $w_{lI} \leq 0$.

In the case of a constant external input, $h_l(\mathbf{r}) = \bar{h}_l$, there exists at least one fixed point solution $a_l(\mathbf{r}) = \bar{a}_l$ of equation (1.4), where

$$\bar{a}_l = \tau\sum_{m=E,I} W_{lm}\sigma(\bar{a}_m) + \bar{h}_l \qquad (1.5)$$

and $W_{lm} = \int_{\mathbf{R}^2} w_{lm}(\mathbf{r})d\mathbf{r}$. If $\bar{h}_l$ is sufficiently small relative to the threshold $\kappa$ then this fixed point is unique and stable. Under the change of coordinates $a_l \to a_l - \bar{h}_l$, it can be seen that the effect of $\bar{h}_l$ is to shift the threshold by the amount $-\bar{h}_l$. Thus there are two ways to increase the excitability of the network and thus destabilize the fixed point: either by increasing the external input $\bar{h}_l$ or reducing the threshold $\kappa$. The latter can occur through the action of drugs on certain brain stem nuclei which, as we shall see, provides a mechanism for generating geometric visual hallucinations [22, 11, 12, 14].

The local stability of $(\bar{a}_E, \bar{a}_I)$ is found by linearisation:

$$\frac{\partial b_l(\mathbf{r},t)}{\partial t} = -b_l(\mathbf{r},t) + \mu\sum_{m=E,I}\int_{\mathbf{R}^2} w_{lm}(|\mathbf{r}-\mathbf{r}'|)b_m(\mathbf{r}',t)d\mathbf{r}' \qquad (1.6)$$

where $b_l(\mathbf{r},t) = a_l(\mathbf{r},t) - \bar{a}_l$ and we have performed a rescaling of the local weights $\tau\sigma'(\bar{a}_l)w_{lm} \to \mu w_{lm}$ with $\mu$ a measure of the degree of network excitability. We have also rescaled $t$ in units of the membrane time constant

$\tau$. Assuming solutions of the form $b_l(\mathbf{r}, t) = b_l(\mathbf{r})e^{-\lambda t}$ we are left with the eigenvalue problem:

$$\lambda b_l(\mathbf{k}) = -b_l(\mathbf{k}) + \mu \sum_m W_{lm}(|\mathbf{k}|^2)b_m(\mathbf{k}) \qquad (1.7)$$

where $b_l(\mathbf{k})$ and $W_{lm}(|\mathbf{k}|^2)$ are, respectively, the Fourier coefficients of $b_l(\mathbf{r})$ and $w_{lm}(\mathbf{r})$. This leads to the matrix *dispersion relation* for $\lambda$ as a function of $q = |\mathbf{k}|$ given by solutions of the characteristic equation

$$\det([\lambda + 1]I - \mu \mathbf{W}(q)) = 0 \qquad (1.8)$$

where $\mathbf{W}$ is the matrix of Fourier coefficients of the $w_{lm}$. One can actually simplify the formulation by reducing eqns. (1.4) to an equivalent one–population model:

$$\tau \frac{\partial a(\mathbf{r}, t)}{\partial t} = - a_l(\mathbf{r}, t) + \tau \int_{\mathbf{R}^2} w(|\mathbf{r} - \mathbf{r}'|)\sigma[a(\mathbf{r}', t)]d\mathbf{r}'$$
$$+ h(\mathbf{r}, t) \qquad (1.9)$$

from which we obtain the dispersion relation $\lambda = -1 + \mu W(q) \equiv \lambda(q)$, with $W(q)$ the Fourier transform of $w(\mathbf{r})$.
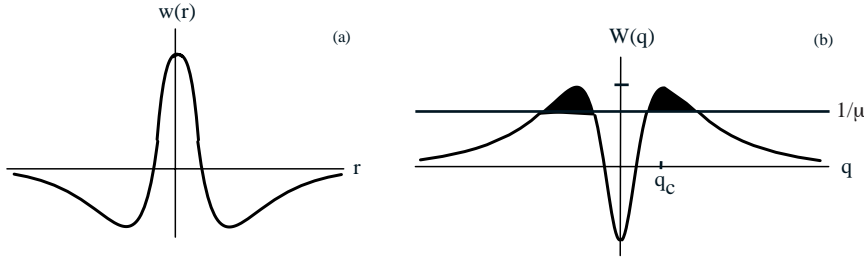


**Figure 1.6.** Neural basis of the Turing mechanism. (a) Mexican hat interaction function showing short-range excitation and long-range inhibition. (b) Fourier transform $W(q)$ of Mexican hat function. There exists a critical parameter $\mu_c = W(q_c)^{-1}$ where $W(q_c) = [\max_q\{W(q)\}]$ such that for $\mu_c < \mu < \infty$ the homogeneous fixed point is unstable.

In either case it is relatively straightforward to set up the conditions under which the homogeneous state first loses its stability at $\mu = \mu_c$ and at a wave–vector with $q = q_c \neq 0$. In the case of equation (1.9) the condition is that $W(q)$ be *bandpass*. This can be achieved with the "Mexican Hat" function (see figure 1.6):

$$w(|\mathbf{r}|) = (\frac{a_+}{\sigma_+})e^{-r^2/\sigma_+^2} - (\frac{a_-}{\sigma_-})e^{-r^2/\sigma_-^2} \qquad (1.10)$$

the Fourier transform of which is:

$$W(q) = \frac{1}{2}(a_+ e^{-\frac{1}{4}\sigma_+^2 q^2} - a_- e^{-\frac{1}{4}\sigma_-^2 q^2}). \tag{1.11}$$

Evidently $W(0) = (1/2)(a_+ - a_-)$ and $W(\infty) = 0$. It is simple to establish that $\lambda$ passes through zero at the critical value $\mu_c$ signalling the growth of spatially periodic patterns with wavenumber $q_c$, where $W(q_c) = \max_q\{W(q)\}$. Close to the bifurcation point these patterns can be represented as linear combinations of plane waves

$$b(\mathbf{r}) = \sum_n (c_n e^{i\mathbf{k}_n \cdot \mathbf{r}} + c_n^* e^{-i\mathbf{k}_n \cdot \mathbf{r}})$$

where the sum is over all wave vectors with $|\mathbf{k}_n| = q_c$ and $n$ can be bounded by restricting the solutions to doubly–periodic patterns in $\mathbf{R}^2$. Depending on the boundary conditions various patterns of stripes or spots can be obtained as solutions. Figure 1.7 shows, for example, a late stage in the development of stripes [62]. Amplitude equations for the coefficients $c_n$ can then be obtained in the usual fashion to determine the linear stability of the various solutions. This analysis of the Wilson–Cowan equations was first carried out by Ermentrout and Cowan as part of their theory of visual hallucinations [22], and is an exact parallel of Turing's original analysis, although he did not develop amplitude equations for the various solutions.
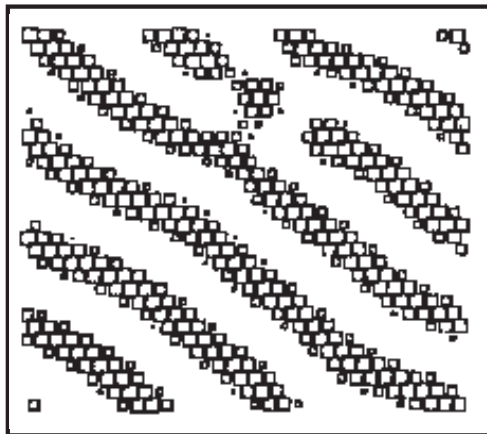


**Figure 1.7.** A late stage in the spontaneous formation of stripes of neural activity. See text for details.

Essentially the same analysis can be applied to a variety of problems concerning the neural development of the various feature maps and connectivity patterns highlighted in § 1.1. Consider, for example, the development

of topographic maps from eye to brain [61, 63]. Such maps develop by a process which involves both genetic and epigenetic factors. Thus the actual growth and decay of connections is epigenetic, involving synaptic plasticity. However the final solution is constrained by genetic factors, which act, so to speak, as boundary conditions. The key insight was provided by von der Malsburg [60] who showed that pattern formation can occur in a developing neural network whose synaptic connectivity or weight matrix is activity dependent and modifiable, provided some form of *competition* is present. Thus Haüssler and von der Malsburg formulated the topographic mapping problem (in the case of a one-dimensional cortex) as follows [30]. Let $w_{rs}$ be the weight of connections from the retinal point $r$ to the cortical point $s$, and $\mathbf{w}$ the associated weight matrix. An evolution equation for $\mathbf{w}$ embodying synaptic plasticity and competition can then be written as

$$\frac{d\mathbf{w}}{dt} = \alpha\mathbf{J} + \beta\mathbf{w} \cdot C(\mathbf{w}) - \mathbf{w} \cdot B(\alpha\mathbf{J} + \beta\mathbf{w} \cdot C(\mathbf{w})) \qquad (1.12)$$

where $\mathbf{J}$ is a matrix with all elements equal to unity, $C_{rs}(\mathbf{x}) = \sum_{r's'} c(r - r', s - s')x_{r's'}$, and

$$B_{rs}(\mathbf{x}) = \frac{1}{2}\left(\frac{1}{N}\sum_{r'} x_{r's} + \frac{1}{N}\sum_{s'} x_{rs'}\right).$$

One can easily show that $\mathbf{w} = \mathbf{J}$ is an unstable fixed point of eqn (1.12). Linearising about this fixed point leads to the linear equation:

$$\frac{d\mathbf{v}}{dt} = \alpha\mathbf{v} + C(\mathbf{v}) - B(\mathbf{v}) - B[C(\mathbf{v})] \qquad (1.13)$$

where $\mathbf{v} = \mathbf{w} - \mathbf{J}$. Since $B$ and $C$ are linear operators, we can rewrite eqn (1.13) in the form:

$$\tau\frac{d\mathbf{v}}{dt} = -\mathbf{v} + \tau(I - B)[(I + C)(\mathbf{v})] \qquad (1.14)$$

where the time constant $\tau = (1 - \alpha)^{-1}$. It is not too difficult to see that the term $(I - B)[(I + C)(\mathbf{v})]$ is equivalent to the action of an effective convolution kernel of the form:

$$w(\mathbf{r}) = w_+(\mathbf{r}) - w_-(\mathbf{r})$$

so that eqn. (1.14) can be rewritten in the familiar form:

$$\tau\frac{\partial\mathbf{v}(\mathbf{r}, t)}{\partial t} = -\mathbf{v}(\mathbf{r}, t) + \tau\int_{\mathbf{R}^2} w(\mathbf{r} - \mathbf{r}')\mathbf{v}(\mathbf{r}', t)d\mathbf{r}' \qquad (1.15)$$

where in this case $\mathbf{r} = \{r, s\}$ and $\mathbf{v}$ is a matrix. Once again there is a dis-
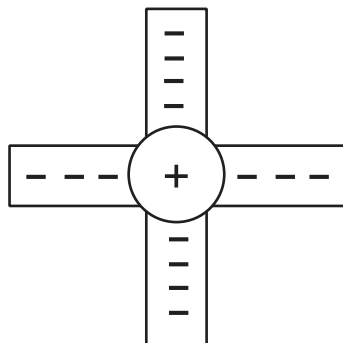
**Figure 1.8.** Structure of the weight kernel $w(r,s)$.

persion relation of the form $\lambda = -1 + \mu W(\mathbf{k}) \equiv \lambda(\mathbf{k})$, where $\mathbf{k} = \{k, l\}$ and, as in the previous examples, assuming appropriate boundary conditions–in this case periodic–it is the Fourier transform $W(\mathbf{k})$ that determines which of the eigenmodes

$$\sum_{kl} c_{kl} e^{i\frac{2\pi}{N}(kr+ls)},$$

emerges at the critical wavenumber $\mathbf{k}_c = \{k_c, l_c\}$. Figure (1.8) shows the form of $w(r,s)$ in the $r-s$ plane. It will be seen that it is similar to the Mexican Hat except that the inhibitory surround is in the form of a cross. This forces the eigenmodes that emerge from the Turing instability to be diagonal in the $r-s$ plane. If the wavenumber is selected so that only one wave is present, this corresponds to an ordered retino–cortical map. Figure 1.9 shows details of the emergence of the required mode.
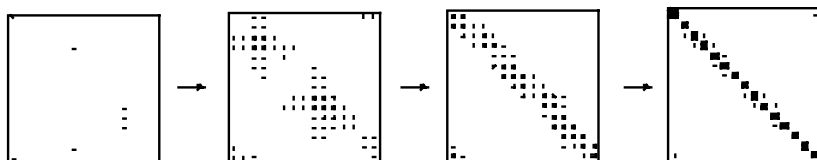


**Figure 1.9.** Stages in the development of an ordered retinotopic map. A single stripe develops in the $r-s$ plane

A second example is to be found in models for the development of ocular dominance maps [53]. Let $n_R(\mathbf{r}, t)$ and $n_L(\mathbf{r}, t)$ be, respectively, the (normalized) right and left eye densities of synaptic connections to

the visual cortex modelled as a two–dimensional sheet. Such densities are presumed to evolve according to an evolution equation of the form:

$$\frac{\partial u_l(\mathbf{r},t)}{\partial t} = \sum_{m=R,L} \int_{\mathbf{R}^2} w_{lm}(|\mathbf{r}-\mathbf{r}'|)\sigma[u_m(\mathbf{r}',t)]d\mathbf{r}' \qquad (1.16)$$

where $u_l = \log\frac{n_l}{1-n_l}$ such that $\sigma(u_l) = n_l$ and the coupling matrix $\mathbf{w}$ is given by

$$\mathbf{w}(r) = w(r)\left(\begin{array}{cc} +1 & -1 \\ -1 & +1 \end{array}\right),$$

With the additional constraint $n_R + n_L = 1$, equation (1.16) reduces to the one–dimensional form:

$$\frac{\partial u_R(\mathbf{r},t)}{\partial t} = 2\int_{\mathbf{R}^2} w(|\mathbf{r}-\mathbf{r}'|)\sigma[u_R(\mathbf{r}',t)]d\mathbf{r}' - \int_{\mathbf{R}^2} w(|\mathbf{r}'|)d\mathbf{r}'. \quad (1.17)$$

which can be rewritten in terms of the variable $n_R(\mathbf{r},t)$ as:

$$\frac{\partial n_R(\mathbf{r},t)}{\partial t} = n_R(\mathbf{r},t)(1 - n_R(\mathbf{r},t))$$

$$[2\int_{\mathbf{R}^2} w(|\mathbf{r}-\mathbf{r}'|)n_R(\mathbf{r}',t)d\mathbf{r}' - \int_{\mathbf{R}^2} w(|\mathbf{r}'|)d\mathbf{r}']. \quad (1.18)$$

The fixed points of this equation are easily seen to be $n_R(\mathbf{r}) = 0, 1$ and $n_R(\mathbf{r}) = \frac{1}{2}$. The first two fixed points are stable, however the third fixed point is unstable to small perturbations. Linearizing about this fixed point we find the dispersion relation $\lambda = \frac{1}{2}W(|\mathbf{k}|)$. Once again the Fourier transform of the interaction kernel $w(|\mathbf{r}|)$ controls the emergence of the usual eigenmodes, in this case plane waves of the form $e^{i\mathbf{k}\cdot\mathbf{r}}$ in the cortical plane. Note that the fixed point $n_R = n_L = \frac{1}{2}$ corresponds to the fixed point $u_R = u_L = 0$ which is a point of reflection symmetry for the function $\sigma[u]$. It is this additional symmetry which results in the emergence of stripes rather than spots or blobs when the fixed point destabilizes.

There are many other examples of the role of the Turing instability in visual neuroscience such as the Marr–Poggio model of stereopsis [41] and the Swindale model for the development of iso–orientation patches [54]. However, all of the neural models involve the same basic mechanism of competition between excitation and inhibition (the Mexican hat form of interaction, see figure 1.6), and most have some underlying symmetry that plays a crucial role in the selection and stability of the resulting patterns. In what follows, we shall develop these ideas further by considering in detail our own recent work on spontaneous pattern formation in primary visual cortex [11, 12, 14]. In this work we have investigated how correlations between the pattern of patchy lateral connections and the underlying orientation map within V1 (as highlighted in § 1.1) effect the large-scale
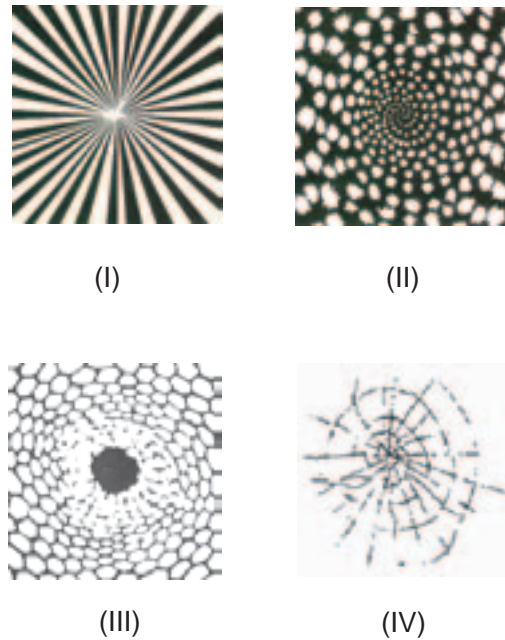
**Figure 1.10.** Hallucinatory form constants. (a) funnel and (b) spiral images seen following ingestion of LSD [redrawn from [50]], (c) honeycomb generated by marihuana [redrawn from [17]], (d) cobweb petroglyph [redrawn from [44]].

dynamics of V1 idealized as a continuous two-dimensional sheet of interacting hypercolumns [11, 12, 14]. We have shown that the patterns of lateral connection are invariant under the so-called *shift-twist* action of the planar Euclidean group $\mathbf{E}(2)$ acting on the product space $\mathbf{R}^2 \times \mathbf{S}^1$. By virtue of the anisotropy of the lateral connections (see figure 1.5), this shift-twist symmetry supports distinct scalar and pseudoscalar group representations of $\mathbf{E}(2)$ [8], which characterize the type of cortical activity patterns that arise through spontaneous symmetry breaking [11]. Following on from the original work of Ermentrout and Cowan [22], we have used our continuum model to develop a theory for the generation of geometric visual hallucinations, based on the idea that some disturbance such as a drug or flickering light can destabilize V1 inducing a spontaneous pattern of cortical activity that reflects the underlying architecture of V1. These activity patterns are seen as hallucinatory images in the visual field, whose spatial scale is determined by the range of lateral connections and the cortical-retinotopic map. Four examples of common hallucinatory images that are reproduced by our model [11] are shown in figure 1.10. Note the contoured nature

of the third and fourth images, which could not have been generated in the original Ermentrout-Cowan model [22]. Our results suggest that the circuits in V1 that are normally involved in the detection of oriented edges and in the formation of contours, are also responsible for the generation of simple hallucinations.

## 1.3 A continuum model of V1 and its intrinsic circuitry

Consider a local population of excitatory ($E$) and inhibitory ($I$) cells at cortical position $\mathbf{r} \in \mathbf{R}^2$ with orientation preference $\phi$. We characterize the state of the population at time $t$ by the real-valued activity variable $a_l(\mathbf{r}, \phi, t)$ with $l = E, I$. As in § 1.2, V1 is treated as an (unbounded) continuous two-dimensional sheet of nervous tissue with the additional simplifying assumption that $\phi$ and $\mathbf{r}$ are independent variables – all possible orientations are represented at every position. Hence, one interpretation of our model would be that it is a continuum version of a lattice of hypercolumns. An argument for the validity of this continuum model is to note that the separation of two points in the visual field—visual *acuity*—(at a given retinal eccentricity of $\mathbf{r}^o$), corresponds to hypercolumn spacing [34], and so to each location in the visual field there corresponds a representation in V1 of that location with finite resolution and all possible orientations. Our large-scale model of V1 takes the form

$$\frac{\partial a_l(\mathbf{r}, \phi, t)}{\partial t} = -a_l(\mathbf{r}, \phi, t) + h_l(\mathbf{r}, \phi, t) \qquad (1.19)$$
$$+ \sum_{m=E,I} \int_{\mathbf{R}^2} \int_0^\pi w_{lm}(\mathbf{r}, \phi | \mathbf{r}', \phi') \sigma[a_m(\mathbf{r}', \phi', t)] \frac{d\phi'}{\pi} d\mathbf{r}'$$

which is a generalized version of the Wilson–Cowan equations of nerve tissue introduced in § 1.2, with $t$ measured in units of $\tau$. The distribution $w_{lm}(\mathbf{r}, \phi | \mathbf{r}', \phi')$ represents the strength or *weight* of connections from the iso-orientation patch $\phi'$ at cortical position $\mathbf{r}'$ to the orientation patch $\phi$ at position $\mathbf{r}$.

Motivated by experimental observations concerning the intrinsic circuitry of V1 (see § 1.1), we decompose $w$ in terms of *local* connections from elements within the same hypercolumn, and patchy excitatory *lateral* connections from elements in other hypercolumns:

$$w_{lm}(\mathbf{r}, \phi | \mathbf{r}', \phi') = w_{loc}(\phi | \phi')\delta(\mathbf{r} - \mathbf{r}') + \varepsilon w_{lat}(\mathbf{r}, \phi | \mathbf{r}', \phi')\delta_{m,E}\beta_l$$
$$(1.20)$$

where $\varepsilon$ is a parameter that measures the weight of lateral relative to local connections. Observations by [31] suggest that $\varepsilon$ is small and therefore

that the lateral connections modulate rather than drive V1 activity. Note that although the lateral connections are excitatory [47, 26], 20% of the connections in layers II and III of V1 end on inhibitory interneurons, so the overall action of the lateral connections can become inhibitory, especially at high levels of activity [31]. The relative strengths of the lateral inputs into local excitatory and inhibitory populations are represented by the factors $\beta_l$.

The local weight distribution is taken to be homogeneous, that is,

$$w_{loc}(\phi|\phi') = W(\phi - \phi') \tag{1.21}$$

for some $\pi$-periodic, even function $W$. It follows that an isolated hypercolumn (zero lateral interactions) has internal $\mathbf{O}(2)$ symmetry corresponding to rotations and reflections within the ring. In order to incorporate the anisotropic nature of the lateral connections, we further decompose $w_{lat}$ as [12]

$$w_{lat}(\mathbf{r}, \phi|\mathbf{r}', \phi') = J(T_{-\phi}(\mathbf{r} - \mathbf{r}'))\delta(\phi - \phi') \tag{1.22}$$

where

$$J(\mathbf{r}) = \int_{-\pi/2}^{\pi/2} p(\eta) \int_{-\infty}^{\infty} g(s)\delta(\mathbf{r} - s\mathbf{e}_\eta)dsd\eta \tag{1.23}$$

with $\mathbf{e}_\eta = (\cos(\eta), \sin(\eta))$, $p(-\eta) = p(\eta)$ and $T_\phi$ the rotation matrix

$$T_\phi \begin{pmatrix} x \\ y \end{pmatrix} = \begin{pmatrix} \cos\phi & -\sin\phi \\ \sin\phi & \cos\phi \end{pmatrix} \begin{pmatrix} x \\ y \end{pmatrix}.$$

Such a distribution links neurons with the same orientation and spatial frequency label, with the function $p(\eta)$ determining the degree of spatial spread (anisotropy) in the pattern of connections relative to the direction of their common orientation preference. The weighting function $g(s)$ specifies how the strength of interaction varies with the distance of separation. A simplified schematic representation of the pattern of lateral connections is illustrated for our coupled hypercolumn model in figure 1.11.

Substituting equations (1.20) and (1.22) back into equation (1.19) leads to the evolution equation

$$\frac{\partial a_l(\mathbf{r}, \phi, t)}{\partial t} = -a_l(\mathbf{r}, \phi, t) + \sum_m \int W_{lm}(\phi - \phi')\sigma[a_m(\mathbf{r}', \phi', t)]\frac{d\phi'}{\pi} \tag{1.24}$$

$$+ \varepsilon\beta_l \int_{-\pi/2}^{\pi/2} p(\eta) \int_{-\infty}^{\infty} g(s)\sigma[a_E(\mathbf{r} + s\mathbf{e}_{\eta+\phi}, \phi, t)]d\eta ds + h_l(\mathbf{r}, \phi, t)$$

If $p(\eta) = 1/\pi$ for all $\eta$ then the weight distribution is isotropic and the system (1.24) is equivariant with respect to $\mathbf{E}(2) \times \mathbf{O}(2)$, where $\mathbf{E}(2)$ denotes
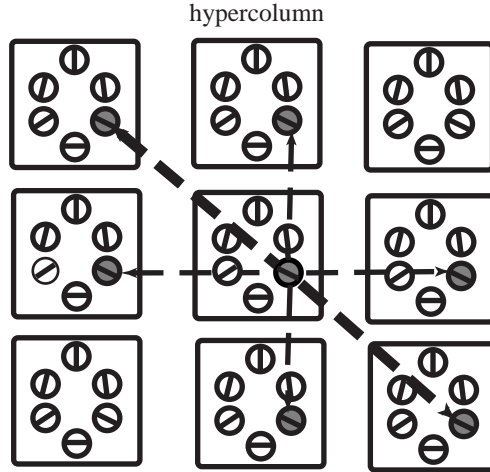
hypercolumn



**Figure 1.11.** Schematic diagram of a coupled hypercolumn model of V1. It is assumed that there are isotropic local interactions within a hypercolumn, and anisotropic lateral interactions between hypercolumns. The latter connect iso-orientation patches located within some angular distance from the visuo-topic axis parallel to their (common) orientation preference (as illustrated for the shaded patches).

the Euclidean group of translations, rotations and reflections in the cortex, and $\mathbf{O}(2)$ is the internal symmetry group of an isolated hypercolumn. It is important to emphasize that cortical rotations are distinct from rotations in the visual field (which correspond to vertical translations in cortex), as well as from internal rotations with respect to orientation. When $p(\eta)$ is non-uniform, the resulting anisotropy breaks both cortical and internal $\mathbf{O}(2)$ symmetries. However, full Euclidean symmetry, $\mathbf{E}(2) = \mathbf{R}^2 \dot{+} \mathbf{O}(2)$, is recovered by considering the combined Euclidean action on $\{\mathbf{r}, \phi\}$, which introduces a form of *shift-twist* symmetry in the plane [18, 11, 12, 67]. More specifically, the anisotropic weight distribution (1.22) is invariant with respect to the following action of the Euclidean group:

$$\begin{aligned}
\mathbf{s} \cdot (\mathbf{r}, \phi) &= (\mathbf{r} + \mathbf{s}, \phi) \quad \mathbf{s} \in \mathbf{R}^2 \\
\xi \cdot (\mathbf{r}, \phi) &= (T_\xi \mathbf{r}, \phi + \xi) \quad \xi \in S^1 \\
\kappa \cdot (\mathbf{r}, \phi) &= (\kappa \mathbf{r}, -\phi)
\end{aligned} \tag{1.25}$$

where $\kappa$ is the reflection $(x_1, x_2) \mapsto (x_1, -x_2)$. The corresponding group action on a function $a : \mathbf{R}^2 \times S \to \mathbf{R}$ is given by

$$\gamma \cdot a(P) = a(\gamma^{-1} \cdot P) \quad \text{for all } \gamma \in \mathbf{R}^2 \dot{+} \mathbf{O}(2) \tag{1.26}$$

and the invariance of $w_{lat}(P|P')$ is expressed as

$$\gamma \cdot w_{lat}(P|P') = w_{lat}(\gamma^{-1} \cdot P|\gamma^{-1} \cdot P') = w_{lat}(P|P').$$

It can be seen that the rotation operation comprises a translation or shift of the orientation preference label $\phi$ to $\phi + \xi$, together with a rotation or twist of the position vector $\mathbf{r}$ by the angle $\xi$. Such an operation provides a novel way to generate the Euclidean group $\mathbf{E}(2)$ of rigid motions in the plane. The fact that the weighting functions are invariant with respect to this form of $\mathbf{E}(2)$ has important consequences for the global dynamics of V1 in the presence of anisotropic lateral connections [11, 12].

## 1.4   Orientation tuning and O(2) symmetry

In the absence of lateral connections ($\varepsilon = 0$) each hypercolumn is independently described by the so-called ring model of orientation tuning [52, 3, 4, 42, 10], in which the internal structure of a hypercolumn is idelaized as a ring of orientation selective cells. That is, equation (1.19) reduces to

$$\frac{\partial a_l}{\partial t} = -a_l + \sum_{m=E,I} W_{lm} * \sigma(a_m) + h_l \tag{1.27}$$

where $*$ indicates a convolution operation

$$W * f(\phi) = \int_{-\pi/2}^{\pi/2} W(\phi - \phi')f(\phi')\frac{d\phi'}{\pi} \tag{1.28}$$

Just as in § 1.2 the local stability of $(\bar{a}_E, \bar{a}_I)$ is found by linearization about the fixed points $\bar{a}_l$ :

$$\frac{\partial b_l}{\partial t} = -b_l + \mu \sum_m W_{lm} * b_m \tag{1.29}$$

where $b_l(\mathbf{r}, \phi, t) = a_l(\mathbf{r}, \phi, t) - \bar{a}_l$. Equation (1.29) has solutions of the form

$$b_l(\mathbf{r}, \phi, t) = B_l e^{\lambda t} \left[ z(\mathbf{r})e^{2in\phi} + \overline{z}(\mathbf{r})e^{-2in\phi} \right] \tag{1.30}$$

where $z(\mathbf{r})$ is an arbitrary (complex) amplitude with complex conjugate $\overline{z}(\mathbf{r})$, and $\lambda$ satisfies the eigenvalue equation

$$(1 + \lambda)\mathbf{B} = \mu \widetilde{\mathbf{W}}(n)\mathbf{B} \tag{1.31}$$

Here $\widetilde{W}_{lm}(n)$ is the $n$th Fourier coefficient in the expansion of the $\pi$-periodic weights kernels $W_{lm}(\phi)$:

$$W_{lm}(\phi) = \widetilde{W}_{lm}(0) + 2\sum_{n=1}^{\infty} \widetilde{W}_{lm}(n)\cos(2n\phi), \quad l, m = E, I \tag{1.32}$$

It follows that

$$\lambda_n^{\pm} = -1 + \mu W_n^{\pm} \tag{1.33}$$

for integer $n$, where

$$W_n^{\pm} = \frac{1}{2}\left[\widetilde{W}_{EE}(n) + \widetilde{W}_{II}(n) \pm \Sigma(n)\right] \tag{1.34}$$

are the eigenvalues of the weight matrix with

$$\Sigma(n) = \sqrt{[\widetilde{W}_{EE}(n) - \widetilde{W}_{II}(n)]^2 + 4\widetilde{W}_{EI}(n)\widetilde{W}_{IE}(n)} \tag{1.35}$$

The corresponding eigenvectors (up to an arbitrary normalization) are

$$\mathbf{B}_n^{\pm} = \begin{pmatrix} -\widetilde{W}_{EI}(n) \\ \frac{1}{2}\left[\widetilde{W}_{EE}(n) - \widetilde{W}_{II}(n) \mp \Sigma(n)\right] \end{pmatrix} \tag{1.36}$$

Equation (1.33) implies that, for sufficiently small $\mu$ (low network excitability), $\lambda_n^{\pm} < 0$ for all $n$ and the homogeneous resting state is stable. However, as $\mu$ increases an instability can occur leading to the spontaneous formation of an orientation tuning curve.

For the sake of illustration, suppose that the Fourier coefficients are given by the Gaussians

$$\widetilde{W}_{lm}(n) = \alpha_{lm}e^{-n^2\xi_{lm}^2/2}, \tag{1.37}$$

with $\xi_{lm}$ determining the range of the axonal fields of the excitatory and inhibitory populations. We consider two particular cases.
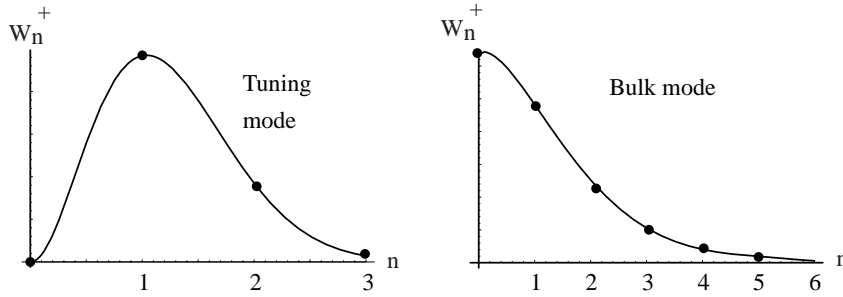


**Figure 1.12.** Spectrum $W_n^{+}$ of local weight distribution with (a) a maximum at $n = 1$ (tuning mode) and (b) a maximum at $n = 0$ (bulk mode).

*Case A*   If $\widetilde{W}_{EE}(n) = \widetilde{W}_{IE}(n)$ and $\widetilde{W}_{II}(n) = \widetilde{W}_{EI}(n)$ for all $n$, then $W_n^- = 0$ and

$$W_n^+ = \alpha_{EE}e^{-n^2\xi_{EE}^2/2} - \alpha_{II}e^{-n^2\xi_{II}^2/2} \qquad (1.38)$$

Suppose that $\xi_{II} > \xi_{EE}$ and $0 < \alpha_{II} < \alpha_{EE}$. As we described in § 1.2 the resulting combination of short range excitation and longer range inhibition generates a Turing instability. Of particular relevance to orientation tuning is the case where $W_n^+$ has a unique (positive) maximum at $n = 1$ (see figure 1.12a). The homogeneous state then destabilizes at the critical point $\mu = \mu_c \equiv 1/W_1^+$ due to excitation of the eigenmodes $\mathbf{b}(\mathbf{r}, \phi, t) = \mathbf{B}a(\mathbf{r}, \phi, t)$ with $\mathbf{B} = (1, 1)^T$ and

$$a(\mathbf{r}, \phi, t) = z(\mathbf{r})e^{2i\phi} + \overline{z}(\mathbf{r})e^{-2i\phi} = |z(\mathbf{r})|\cos(2[\phi - \phi^*(\mathbf{r})]) \quad (1.39)$$

with $z(\mathbf{r}) = |z(\mathbf{r})|e^{-2i\phi^*(\mathbf{r})}$. Since these modes have a single maximum in the interval $(-90^o, 90^o)$, each hypercolumn supports an activity profile consisting of a solitary peak centred about $\phi^*(\mathbf{r}) = \arg z(\mathbf{r})$. It can be
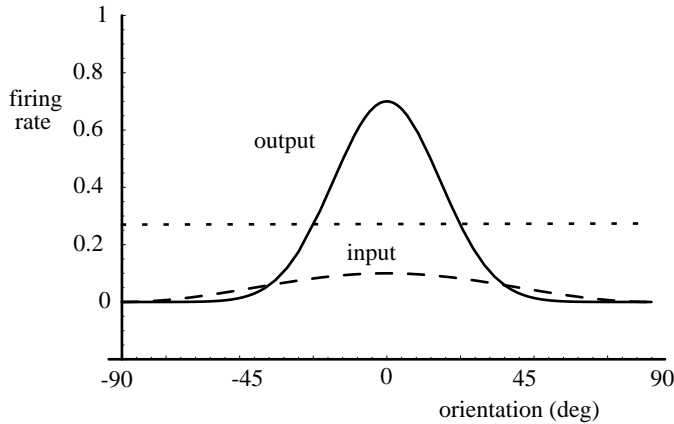


**Figure 1.13.** Sharp orientation tuning curve in a single hypercolumn. Local recurrent excitation and inhibition amplifies a weakly modulated input from the LGN. Dotted line is the base–line output without orientation tuning.

shown that the saturating nonlinearities of the system stabilize the tuning curves beyond the critical point $\mu_c$ [23, 10] – see also § 1.5.2. The location of the peak $\phi^*(\mathbf{r})$ of the tuning curve at $\mathbf{r}$ is arbitrary in the presence of constant inputs, reflecting the hidden **O**(2) symmetry of a hypercolumn. However, the inclusion of an additional small amplitude input $\Delta h_l(\mathbf{r}, \phi) \sim \cos[2(\phi - \Phi(\mathbf{r}))]$ breaks this symmetry, and locks the location

of the tuning curve at each point $\mathbf{r}$ to the orientation corresponding to the peak of the local stimulus, that is, $\phi^*(\mathbf{r}) = \Phi(\mathbf{r})$. As one moves further away from the point of instability, the amplitude of the tuning curve increases and sharpening occurs due to the nonlinear effects of the firing rate function (1.3). This is illustrated in figure 1.13, where the input and output (normalized) firing rate of the excitatory population of a single hypercolumn are shown. Thus the local intracortical connections within a hypercolumn serve both to amplify and sharpen a weakly oriented input signal from the LGN [52, 4]. On the other hand, if the local level of inhibition is reduced such that $\alpha_{II} \ll \alpha_{EE}$, then $W_n^+$ is a monotonically decreasing function of $|n|$ (see figure 1.12b), and the homogeneous fixed point undergoes a bulk instability resulting in broadening of the tuning curve. This is consistent with experimental data demonstrating a loss of stable orientation tuning in cats with blocking of intracortical inhibition [45][2].

*Case B*   If $\Sigma(n)$ is pure imaginary, $\Sigma(n) = i\Omega(n)$, then

$$W_n^\pm = \alpha_{EE}\mathrm{e}^{-n^2\xi_{EE}^2/2} - \alpha_{II}\mathrm{e}^{-n^2\xi_{II}^2/2} \pm i\Omega(n) \qquad (1.40)$$

Assume, as in case A, that the difference of Gaussians has a maximum at $n = 1$. Then an instability will occur at the critical point $\mu_c = 1/\Re(W_1^+)$ due to excitation of the oscillatory eigenmodes

$$\mathbf{b}(\mathbf{r}, \phi, t) = \left[ z_L(\mathbf{r})\mathrm{e}^{i(\Omega_0 t - 2\phi)} + z_R(\mathbf{r})\mathrm{e}^{i(\Omega_0 t + 2\phi)} \right] \mathbf{B} + c.c. \qquad (1.41)$$

where $\Omega_0 = \mu_c\Omega(1)$ and $\mathbf{B} = \mathbf{B}_1^+$. It is then possible for rotating tuning curves to be generated spontaneously within a hypercolumn [4].

## 1.5   Amplitude equation for interacting hypercolumns

An isolated hypercolumn exhibits spontaneous $\mathbf{O}(2)$ symmetry breaking leading to the formation of an orientation tuning curve. How is this process modulated by anisotropic lateral interactions between hypercolumns? In this section we use perturbation theory to derive a dynamical equation for the complex amplitude $z(\mathbf{r})$ for orientation tuning in the presence of lateral interactions. We will then use this amplitude equation to show how the lateral interactions induce correlations between $z(\mathbf{r})$ at different points in

---

[2]  The idea that local cortical interactions play a role in orientation tuning is still controversial. The classical model of Hubel and Wiesel [32] proposes a very different mechanism, in which both the orientation preference and tuning of a cell arise primarily from the geometrical alignment of the receptive fields of the LGN neurons projecting to it. This has also received recent experimental support [25]. On the other hand, intracellular measurements indicate that direct inputs from the LGN to neurons in layer 4 of V1 provide only a fraction of the total excitatory inputs relevant to orientation tuning [59]

the cortex, leading to spatially periodic patterns of activity across V1 (see § 1.6). These patterns reproduce the commonly found types of geometric visual hallucinations when mapped back into visual field coordinates under the retino cortical map of figure 1.2 (see § 1.6.4). Our basic assumptions in the derivation of the amplitude equation are as follows: (i) each hypercolumn is close to a bifurcation point signalling the onset of sharp orientation tuning and (ii) the interactions between hypercolumns are *weak*.

### 1.5.1 Cubic amplitude equation: stationary case

Let us perform a Taylor expansion of equation (1.24) with $b_l(\mathbf{r}, \phi, t) = a_l(\mathbf{r}, \phi, t) - \bar{a}_l$

$$\frac{\partial b_l}{\partial t} = -b_l + \sum_{m=E,I} W_{lm} * \left[ \mu b_m + \gamma_m b_m^2 + \gamma_m' b_m^3 + \dots \right] + \Delta h_l$$
$$+ \varepsilon \beta_l w_{lat} \circ \left( [\bar{\sigma}_E + \mu b_E + \dots] \right) \tag{1.42}$$

where $\Delta h_l = h_l - \bar{h}_l$ and $\mu = \sigma'(\bar{a}_E)$, $\gamma_l = \sigma''(\bar{a}_l)/2$, $\gamma_l' = \sigma'''(\bar{a}_l)/6$. The convolution operation $*$ is defined by equation (1.28)) and

$$[w_{lat} \circ f](\mathbf{r}, \phi) = \int_{-\pi/2}^{\pi/2} \int_{-\infty}^{\infty} p(\eta) g(s) f(\mathbf{r} + s\mathbf{e}_{\eta+\phi}, \phi) ds d\eta \tag{1.43}$$

for an arbitrary function $f(\mathbf{r}, \phi)$ and $w_{lat}$ given by equation (1.22). Suppose that the system is $\varepsilon$-close to the point of marginal stability of the homogeneous fixed point associated with excitation of the modes $e^{\pm 2i\phi}$. That is, take $\mu = \mu_c + \varepsilon \Delta \mu$ where $\mu_c = 1/W_1^+$, see equation (1.33). Substitute into equation (1.42) the perturbation expansion

$$b_m = \varepsilon^{1/2} b_m^{(1)} + \varepsilon b_m^{(2)} + \varepsilon^{3/2} b_m^{(3)} + \dots \tag{1.44}$$

Finally, introduce a slow time-scale $\tau = \varepsilon t$ and collect terms with equal powers of $\varepsilon$. This leads to a hierarchy of equations of the form (up to $\mathcal{O}(\varepsilon^{3/2})$)

$$[\mathcal{L}\mathbf{b}^{(1)}]_l = 0 \tag{1.45}$$

$$[\mathcal{L}\mathbf{b}^{(2)}]_l = v_l^{(2)} \tag{1.46}$$
$$\equiv \sum_{m=E,I} \gamma_m W_{lm} * [b_m^{(1)}]^2 + \beta_l \bar{\sigma}_E w_{lat} \circ 1$$

$$[\mathcal{L}\mathbf{b}^{(3)}]_l = v_l^{(3)} \tag{1.47}$$
$$\equiv -\frac{\partial b_l^{(1)}}{\partial \tau} + \sum_{m=E,I} W_{lm} * \left[ \Delta \mu b_m^{(1)} + \gamma_m' [b_m^{(1)}]^3 + 2\gamma_m b_m^{(1)} b_m^{(2)} \right]$$
$$+ \mu_c \beta_l w_{lat} \circ b_E^{(1)} + \Delta h_l$$

with the linear operator $\mathcal{L}$ defined according to

$$[\mathcal{L}\mathbf{b}]_l = b_l - \mu_c \sum_{m=E,I} W_{lm} * b_m \tag{1.48}$$

We have also assumed that the modulatory external input is $\mathcal{O}(\varepsilon^{3/2})$ and rescaled $\Delta h_l \to \varepsilon^{3/2}\Delta h_l$

The first equation in the hierarchy, equation (1.45), has solutions of the form

$$\mathbf{b}^{(1)}(\mathbf{r},\phi,\tau) = \left(z(\mathbf{r},\tau)e^{2i\phi} + \overline{z}(\mathbf{r},\tau)\,e^{-2i\phi}\right)\mathbf{B} \tag{1.49}$$

with $\mathbf{B} \equiv \mathbf{B}_1^+$ defined in equation (1.36). We obtain a dynamical equation for the complex amplitude $z(\mathbf{r},\tau)$ by deriving solvability conditions for the higher order equations. We proceed by taking the inner product of equations (1.46) and (1.47) with the dual eigenmode $\widetilde{\mathbf{b}}(\phi) = e^{2i\phi}\widetilde{\mathbf{B}}$ where

$$\widetilde{\mathbf{B}} = \begin{pmatrix} W_{IE}(1) \\ -\frac{1}{2}\left[W_{EE}(1) - W_{II}(1) - \Sigma(1)\right] \end{pmatrix} \tag{1.50}$$

so that

$$[\mathcal{L}^T\widetilde{\mathbf{b}}]_l \equiv \widetilde{b}_l - \mu_c \sum_{m=E,I} W_{ml} * \widetilde{b}_m = 0$$

The inner product of any two vector-valued functions of $\phi$ is defined as

$$\langle \mathbf{u} | \mathbf{v} \rangle = \int_0^\pi \left[\overline{u}_E(\phi)v_E(\phi) + \overline{u}_I(\phi)v_I(\phi)\right]\frac{d\phi}{\pi} \tag{1.51}$$

With respect to this inner product, the linear operator $\mathcal{L}$ satisfies $\langle \widetilde{\mathbf{b}} | \mathcal{L}\mathbf{b} \rangle = \langle \mathcal{L}^T\widetilde{\mathbf{b}} | \mathbf{b} \rangle = 0$ for any $\mathbf{b}$. Since $\mathcal{L}\mathbf{b}^{(p)} = \mathbf{v}^{(p)}$, we obtain a hierarchy of solvability conditions $\langle \widetilde{\mathbf{b}} | \mathbf{v}^{(p)} \rangle = 0$ for $p = 2, 3, \ldots$.

It can be shown from equations (1.43), (1.46) and (1.49) that the first solvability condition is identically satisfied (provided that the system is bifurcating from a uniform state). The solvability condition $\langle \widetilde{\mathbf{b}} | \mathbf{v}^{(3)} \rangle = 0$ generates a cubic amplitude equation for $z(\mathbf{r},\tau)$. As a further simplification we set $\gamma_m = 0$, since this does not alter the basic structure of the amplitude equation. Using equations (1.43), (1.47) and (1.49) we then find that (after rescaling $\tau$)

$$\frac{\partial z(\mathbf{r},\tau)}{\partial \tau} = z(\mathbf{r},\tau)(\Delta\mu - A|z(\mathbf{r},\tau)|^2) + f(\mathbf{r}) \tag{1.52}$$

$$+ \beta \int_0^\pi w_{lat} \circ \left[z(\mathbf{r},\tau) + \overline{z}(\mathbf{r},\tau)e^{-4i\phi}\right]\frac{d\phi}{\pi}$$

where

$$f(\mathbf{r}) = \mu_c \sum_{l=E,I} \widetilde{B}_l \int_0^\pi e^{-2i\phi}\Delta h_l(\mathbf{r},\phi)\frac{d\phi}{\pi} \tag{1.53}$$

and

$$\beta = \frac{\mu_c^2 B_E}{\widetilde{\mathbf{B}}^T \mathbf{B}} \sum_{l=E,I} \beta_l \widetilde{B}_l, \quad A = -\frac{3}{\widetilde{\mathbf{B}}^T \mathbf{B}} \sum_{l=E,I} \widetilde{B}_l \gamma_l' B_l^3 \tag{1.54}$$

Equation (1.52) is our reduced model of weakly interacting hypercolumns. It describes the effects of anisotropic lateral connections and modulatory inputs from the LGN on the dynamics of the (complex) amplitude $z(\mathbf{r}, \tau)$. The latter determines the response properties of the orientation tuning curve associated with the hypercolumn at cortical position $\mathbf{r}$. The coupling parameter $\beta$ is a linear combination of the relative strengths of the lateral connections innervating excitatory neurons and those innervating inhibitory neurons with $D_E, D_I$ determined by the local weight distribution. Since $D_E > 0$ and $D_I < 0$, we see that the effective interactions between hypercolumns have both an excitatory and an inhibitory component.

### 1.5.2   Orientation tuning revisited

In the absence of lateral interactions, equation (1.52) reduces to

$$\frac{\partial z(\mathbf{r}, \tau)}{\partial \tau} = z(\mathbf{r}, \tau)(\Delta\mu - A|z(\mathbf{r}, \tau)|^2) + f(\mathbf{r}) \tag{1.55}$$

For the nonlinear output function (1.3), we find that $A > 0$. Hence, if $f(\mathbf{r}) = 0$ then there exist (marginally) stable time-independent solutions of the form $z(\mathbf{r}) = \sqrt{\Delta\mu/A} e^{-i\phi(\mathbf{r})}$ where $\phi(\mathbf{r})$ is an arbitrary phase that determines the location of the peak of the tuning curve at position $\mathbf{r}$. Now consider the effects of a weakly biased input from the LGN $h_l(\mathbf{r}, \phi, \tau) = C(\mathbf{r}) \cos(2[\phi - \omega\tau])$. This represents a slowly rotating stimulus with angular velocity $\omega$ and contrast $C(\mathbf{r}) = \mathcal{O}(\varepsilon^{3/2})$. Equation (1.53) implies that $f(\mathbf{r}) = C(\mathbf{r}) e^{-2i\omega\tau}$. Writing $z = v e^{-2i(\phi + \omega\tau)}$ we obtain from (1.55) the pair of equations

$$\dot{v} = v(\mu - \mu_c + Av^2) + C\cos(2\phi)$$
$$\dot{\phi} = -\omega - \frac{C}{2v}\sin(2\phi) \tag{1.56}$$

Thus, provided that $\omega$ is sufficiently small, equation (1.56) will have stable fixed point solution $\{v^*(\mathbf{r}), \phi^*(\mathbf{r})\}$ in which the peak of the tuning curve is entrained to the signal. That is, writing $\mathbf{b}^{(1)}(\mathbf{r}, \phi) = \mathbf{B}a(\mathbf{r}, \phi)$,

$$a(\mathbf{r}, \phi) = v^*(\mathbf{r})\cos(2[\phi - \omega\tau - \phi^*(\mathbf{r})]) \tag{1.57}$$

with $\phi^*(\mathbf{r}) = 0$ when $\omega = 0$.

It is also possible to repeat our bifurcation analysis in the case where each hypercolumn undergoes a bulk instability. This occurs, for example,

when the spectrum of local connections is as in figure 1.12b. The amplitude equation (1.52) now takes the form

$$\frac{\partial a(\mathbf{r}, \tau)}{\partial \tau} = a(\mathbf{r}, \tau)(\Delta\mu - Aa(\mathbf{r}, \tau)^2) + f_0(\mathbf{r}) + \beta \int_0^\pi w_{lat} \circ a(\mathbf{r}, \tau)\frac{d\phi}{\pi}$$

(1.58)

with $a$ real and $f_0$ the $\phi$-averaged LGN input. It follows that, in the absence of lateral interactions, each hypercolumn bifurcates to a $\phi$-independent state whose amplitude $a(\mathbf{r})$ is a root of the cubic

$$a(\mathbf{r})(\Delta\mu - Aa(\mathbf{r})^2) + f_0(\mathbf{r}) = 0$$

(1.59)

### 1.5.3  Cubic amplitude equation: oscillatory case

In our derivation of the amplitude equation (1.52) we assumed that the local cortical circuit generates a stationary orientation tuning curve. However, as shown in § 1.4, it is possible for a time-periodic tuning curve to occur when $\Im(W_1^+) \neq 0$. Taylor expanding (1.24) as before leads to the hierarchy of equations (1.45)–(1.47) except that the linear operator $\mathcal{L} \to \mathcal{L}_t = \mathcal{L} + \partial/\partial t$. The lowest order solution (1.49) now takes the form

$$\mathbf{b}^{(1)}(\mathbf{r}, \phi, t, \tau) = \left[z_L(\mathbf{r}, \tau)\mathrm{e}^{i(\Omega_0 t - 2\phi)} + z_R(\mathbf{r}, \tau)\mathrm{e}^{i(\Omega_0 t + 2\phi)}\right]\mathbf{B} + c.c.$$

(1.60)

where $z_L$ and $z_R$ represent the complex amplitudes for anti-clockwise $(L)$ and clockwise $(R)$ rotating waves (around the ring of a single hypercolumn), and $\Omega_0 = \mu_c\Im(\Sigma(1))$. Introduce the generalized inner product

$$\langle \mathbf{u}|\mathbf{v}\rangle = \lim_{T\to\infty} \frac{1}{T}\int_{-T/2}^{T/2}\int_0^\pi [\overline{u}_E(\phi, t)v_E(\phi, t) + \overline{u}_I(\phi, t)v_I(\phi, t)]\frac{d\phi}{\pi}dt$$

(1.61)

and the dual vectors $\widetilde{\mathbf{b}}_L = \overline{\overline{\mathbf{B}}}\mathrm{e}^{i(\Omega_0 t - 2\phi)}$, $\widetilde{\mathbf{b}}_R = \overline{\overline{\mathbf{B}}}\mathrm{e}^{i(\Omega_0 t + 2\phi)}$. Using the fact that $\langle \widetilde{\mathbf{b}}_L|\mathcal{L}_t b\rangle = \langle \widetilde{\mathbf{b}}_R|\mathcal{L}_t \mathbf{b}\rangle = 0$ for arbitrary $\mathbf{b}$ we obtain the pair of solvability conditions $\langle \widetilde{\mathbf{b}}_L|\mathbf{v}^{(p)}\rangle = \langle \widetilde{\mathbf{b}}_R|\mathbf{v}^{(p)}\rangle = 0$ for each $p \geq 2$.

As in the the stationary case, the $p = 2$ solvability conditions are identically satisfied. The $p = 3$ solvability conditions then generate cubic amplitude equations for $z_L, z_R$ of the form

$$\frac{\partial z_L(\mathbf{r}, \tau)}{\partial \tau} = (1 + i\Omega_0)z_L(\mathbf{r}, \tau)(\Delta\mu - A|z_L(\mathbf{r}, \tau)|^2 - 2A|z_R(\mathbf{r}, \tau)|^2)$$

$$+ \beta \int_0^\pi w_{lat} \circ \left[z_L(\mathbf{r}, \tau) + z_R(\mathbf{r}, \tau)\mathrm{e}^{4i\phi}\right]\frac{d\phi}{\pi}$$

(1.62)

and

$$\frac{\partial z_R(\mathbf{r}, \tau)}{\partial \tau} = (1 + i\Omega_0) z_R(\mathbf{r}, \tau)(\Delta\mu - A|z_R(\mathbf{r}, \tau)|^2 - 2A|z_L(\mathbf{r}, \tau)|^2)$$

$$+ \beta \int_0^\pi w_{lat} \circ \left[ z_R(\mathbf{r}, \tau) + z_L(\mathbf{r}, \tau) e^{-4i\phi} \right] \frac{d\phi}{\pi} \qquad (1.63)$$

where

$$f_\pm(\mathbf{r}) = \lim_{T\to\infty} \frac{\mu_c}{T} \int_{-T/2}^{T/2} \int_0^\pi e^{-i(\Omega_0 t \pm 2\phi)} \sum_{l=E,I} \widetilde{B}_l \Delta h_l(\mathbf{r}, \phi, t) \frac{d\phi}{\pi} dt$$

$$(1.64)$$

Note that the amplitudes only couple to time-dependent inputs from the LGN.

## 1.6 Cortical pattern formation and E(2) symmetry

We now use the amplitude equations derived in § 1.5 to investigate how **O**(2) symmetry breaking within a hypercolumn is modified by the presence of anisotropic lateral interactions, and show how it leads to the formation of spatially periodic activity patterns across the cortex that break the underlying **E**(2) symmetry. We begin by considering the case of stationary patterns. Oscillatory patterns will be considered in § 1.6.5.

### 1.6.1 Linear stability analysis

Since we are focusing on spontaneous pattern formation, we shall assume that there are no inputs from the LGN, $f(\mathbf{r}) = 0$. Equation (1.52) then has the trivial solution $z = 0$. Linearizing about this solution gives

$$\frac{\partial z(\mathbf{r}, \tau)}{\partial \tau} = \Delta\mu \, z(\mathbf{r}, \tau) + \beta \int_0^\pi w_{lat} \circ \left[ z(\mathbf{r}, \tau) + \overline{z}(\mathbf{r}, \tau) e^{-4i\phi} \right] \frac{d\phi}{\pi}$$

$$(1.65)$$

If we ignore boundary effects by treating V1 as an unbounded two dimensional sheet, then equation (1.65) has two classes of solution, $z_\pm$, of the form

$$z_+(\mathbf{r}, \tau) = e^{\lambda_+ \tau} e^{-2i\varphi} \left[ c e^{i\mathbf{k}\cdot\mathbf{r}} + \overline{c} e^{-i\mathbf{k}\cdot\mathbf{r}} \right] \qquad (1.66)$$

$$z_-(\mathbf{r}, \tau) = i e^{\lambda_- \tau} e^{-2i\varphi} \left[ c e^{i\mathbf{k}\cdot\mathbf{r}} + \overline{c} e^{-i\mathbf{k}\cdot\mathbf{r}} \right] \qquad (1.67)$$

where $\mathbf{k} = q(\cos(\varphi), \sin(\varphi))$ and $c$ is an arbitrary complex amplitude. Substitution into equation (1.65) and using equation (1.43) leads to the eigenvalue equation

$$\lambda_\pm = \Delta\mu + \beta \int_0^\pi \left[ \int_{-\infty}^\infty g(s) e^{iqs\cos(\phi)} ds \right] \left( 1 \pm \chi e^{-4i\phi} \right) \frac{d\phi}{\pi} \qquad (1.68)$$

where

$$\chi = \int_{-\pi/2}^{\pi/2} p(\eta)e^{-4i\eta}d\eta \tag{1.69}$$

Using an expansion in terms of Bessel functions

$$e^{ix\cos(\phi)} = \sum_{n=-\infty}^{\infty} (-i)^n J_n(x)e^{in\phi} \tag{1.70}$$

the eigenvalue equation reduces to the more compact form

$$\lambda_\pm = \Delta\mu + \beta G_\pm(q) \tag{1.71}$$

with

$$G_\pm(q) = G_0(q) \pm \chi G_2(q) \tag{1.72}$$

and

$$G_n(q) = (-1)^n \int_{-\infty}^{\infty} g(s)J_{2n}(qs)ds \tag{1.73}$$

Before using equation (1.71) to determine how the lateral interactions modify the condition for marginal stability, we need to specify the form of the weight distribution $g(s)$. From experimental data based on tracer injections it appears that the patchy lateral connections extend several mm on either side of a hypercolumn and the field of axon terminals within a patch tends to diminish in size the further away it is from the injection site [47, 26, 66, 40]. The total extent of the connections depends on the particular species under study. In our continuum model we assume that

$$g(s) = e^{-(s-s_0)^2/2\xi^2}\Theta(s - s_0) \tag{1.74}$$

where $\xi$ determines the range and $s_0$ the minimum distance of the (non-local) lateral connections. Recall that there is growing experimental evidence to suggest that lateral connections tend to have an inhibitory effect in the presence of high contrast visual stimuli but an excitatory effect at low contrasts [28]. It is possible that during the experience of hallucinations there are sufficient levels of activity within V1 for the inhibitory effects of the lateral connections to predominate. Many subjects who have taken LSD and similar hallucinogens report seeing bright white light at the centre of the visual field which then explodes into a hallucinatory image in about 3 sec, corresponding to a propagation velocity in V1 of about 2.5 cm per sec. suggestive of slowly moving epileptiform activity [50]. In light of this, we assume that $\beta < 0$ during the experience of a visual hallucination.

In figure 1.14(a) we plot $G_\pm(q)$ as a function of $q$ for the given weight distribution (1.74) and the spread function $p(\eta) = \delta(\eta)$ for which $\chi = 1$.
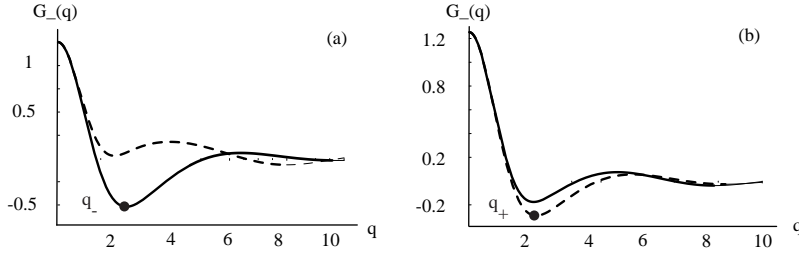
**Figure 1.14.** (a) Plot of functions $G_-(q)$ (solid line) and $G_+(q)$ (dashed line) in the case $\chi = 1$ (strong anisotropy) and $g(s)$ defined by (1.74) for $\xi = 1$ and $s_0 = 1$. The critical wavenumber for spontaneous pattern formation is $q_-$. The marginally stable eigenmodes are odd functions of $\phi$. (b) Same as (a) except that $\chi = \sin 4\eta_0/4\eta_0$ with lateral spread of width $\eta_0 = \pi/3$. The marginally stable eigenmodes are now even functions of $\phi$.

It can be seen that $G_\pm(q)$ has a unique minimum at $q = q_\pm \neq 0$ and $G_-(q_-) < G_+(q_+)$. Since $\beta < 0$ it follows that the homogeneous state $z(\mathbf{r}, \tau) = 0$ becomes marginally stable at the modified critical point $\mu_c' = \mu_c - \varepsilon\beta G_-(q_-)$. The corresponding marginally stable modes are given by combining equations (1.49) and (1.67) for $\lambda_- = 0$. Writing $\mathbf{b}^{(1)}(\mathbf{r}, \phi) = a(\mathbf{r}, \phi)\mathbf{B}$ we have

$$a(\mathbf{r}, \phi) = \sum_{n=1}^{N} c_n e^{i\mathbf{k}_n \cdot \mathbf{r}} \sin(\phi - \varphi_n) + c.c. \tag{1.75}$$

where $\mathbf{k}_n = q_-(\cos\varphi_n, \sin\varphi_n)$ and $c_n$ is a complex amplitude. These modes will be recognized as linear combinations of plane waves modulated by *odd* (phase-shifted) $\pi$-periodic functions $\sin[2(\phi - \varphi_n)]$. The infinite degeneracy arising from rotation invariance means that all modes lying on the circle $|\mathbf{k}| = q_-$ become marginally stable at the critical point. However, this can be reduced to a finite set of modes by restricting solutions to be doubly periodic functions as explained in § 1.6.2.

The solutions (1.75) are precisely the lowest-order odd eigenfunctions derived using the perturbation methods of [11].[3] It is also possible for even (+) eigenmodes to destabilize first when there is a sufficient spread in the

---

[3] Note that in [11] we used a different perturbation scheme in which the strength of lateral connections $\varepsilon$ and the distance from the bifurcation point $\mu - \mu_c$ were taken to be two independent parameters. The linearized equations were first solved using a perturbation expansion in the coupling. Amplitude equations for the linear modes were then derived by carrying out a Poincare-Linstedt expansion with respect to $\mu - \mu_c$. This approach is particularly suitable for studying the role of symmetries in the spontaneous formation of cortical activity patterns underlying visual hallucinations.

distribution of lateral connections about the visuotopic axis as shown in figure 1.11. More specifically, if we take $p(\eta) = \Theta(|\eta| - \eta_0)/2\eta_0$, then

$$G_\pm(q) = G_0(q) \pm \frac{\sin(4\eta_0)}{4\eta_0} G_2(q) \qquad (1.76)$$

such that $G_+(q_+) < G_-(q_-)$ when $\eta_0 > \pi/4$, which is illustrated in figure 1.14(b). It follows that the homogeneous state now becomes marginally stable at the critical point $\mu'_c = \mu_c - \varepsilon\beta G_+(q_+)$ due to excitation of the even modes given by equations (1.49) and (1.66) for $\lambda_+ = 0$:

$$a(\mathbf{r}, \phi) = \sum_{n=1}^{N} c_n e^{i\mathbf{k}_n \cdot \mathbf{r}} \cos(\phi - \varphi_n) + c.c. \qquad (1.77)$$

where $\mathbf{k}_n = q_+(\cos(\varphi_n), \sin(\varphi_n))$.

A third class of solution can occur when each hypercolumn undergoes a bulk instability, as described by the amplitude equation (1.58). Repeating the above linear analysis, we find that there are now only even eigenmodes, which are $\phi$-independent (to leading order), and take the form

$$a(\mathbf{r}) = \sum_{n=1}^{N} [c_n e^{i\mathbf{k}_n \cdot \mathbf{r}} + \bar{c}_n e^{-i\mathbf{k}_n \cdot \mathbf{r}}] \qquad (1.78)$$

The corresponding eigenvalue equation is

$$\lambda = \Delta\mu + G_0(q) \qquad (1.79)$$

with $G_0(q)$ defined in equation (1.73). Thus $|\mathbf{k}_n| = q_0$ where $q_0$ is the minimum of $G_0(q)$.

It follows from our analysis that there are three classes of eigenmode that can bifurcate from the resting state. These are represented, respectively, by linear combinations of one of the three classes of roll pattern shown in figure 1.15. The $m = 0$ roll corresponds to modes of the form (1.78), and consists of alternating regions of high and low cortical activity in which individual hypercolumns do not amplify any particular orientation: the resulting patterns are said to be *non-contoured*. The $m = 1$ rolls correspond to the odd and even oriented modes of equations (1.75) and (1.77). These are constructed using a winner-take-all rule in which only the orientation with maximal response is shown at each point in the cortex (after some coarse-graining). The resulting patterns are said to be *contoured*. The particular class that is selected depends on the detailed structure of the local and lateral weights. The $m = 0$ type will be selected when the local inhibition within a hypercolumn is sufficiently weak, whereas the $m = 1$ type will occur when there is strong local inhibition, with the degree of anisotropy in the lateral connections determining whether the patterns are even or odd.
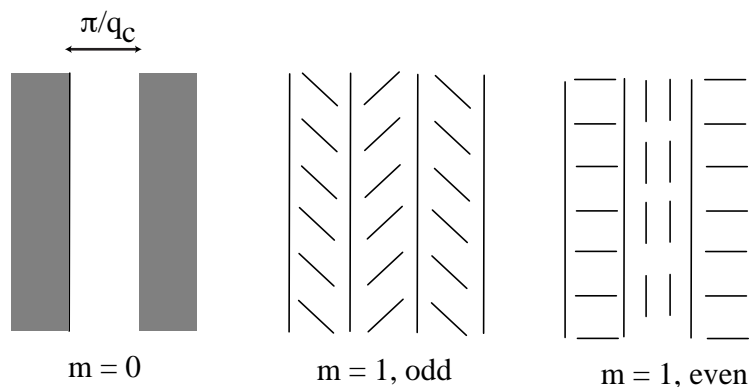
**Figure 1.15.** Three classes of rolls found in cortical pattern formation

### 1.6.2 Doubly-periodic planforms

Rotation symmetry implies that the space of marginally stable modes is infinite-dimensional. That is, all plane-waves with wavevectors **k** lying on the critical circle $|\mathbf{k}| = q_c$ are allowed, with $q_c = q_-$ for odd modes and $q_c = q_+$ for even modes. (For concreteness, we focus on the contoured eigenmodes). However, translation symmetry means that we can restrict the space of solutions to that of doubly periodic functions corresponding to regular tilings of the plane. The associated space of marginally stable eigenmodes is then finite–dimensional. A finite set of specific functions can then be identified as candidate *planforms* in the sense that they approximate time-independent solutions of equation (1.24) sufficiently close to the critical point where the homogeneous state loses stability. These planforms consist of finite linear combinations of one of the three types of stripe pattern shown in figure 1.15.

**Table 1.1.** Generators for the planar lattices and their dual lattices.

| Lattice | $\boldsymbol{\ell}_1$ | $\boldsymbol{\ell}_2$ | $\hat{\boldsymbol{\ell}}_1$ | $\hat{\boldsymbol{\ell}}_2$ |
|---|---|---|---|---|
| Square | $(1,0)$ | $(0,1)$ | $(1,0)$ | $(0,1)$ |
| Hexagonal | $(1,\frac{1}{\sqrt{3}})$ | $(0,\frac{2}{\sqrt{3}})$ | $(1,0)$ | $\frac{1}{2}(-1,\sqrt{3})$ |
| Rhombic | $(1,-\cot\eta)$ | $(0,\csc\eta)$ | $(1,0)$ | $(\cos\eta,\sin\eta)$ |

Let $\mathcal{L}$ be a planar lattice; that is, choose two linearly independent vectors $\boldsymbol{\ell}_1$ and $\boldsymbol{\ell}_2$ and let

$$\mathcal{L} = \{2\pi m_1\boldsymbol{\ell}_1 + 2\pi m_2\boldsymbol{\ell}_2 : m_1, m_2 \in \mathbf{Z}\}.$$

Note that $\mathcal{L}$ is a subgroup of the group of planar translations. A function $f :\to \mathbf{R}$ is *doubly periodic with respect to* $\mathcal{L}$ if

$$f(x + \boldsymbol{\ell}, \phi) = f(x, \phi)$$

for every $\boldsymbol{\ell} \in \mathcal{L}$. Let $\theta$ be the angle between the two basis vectors $\boldsymbol{\ell}_1$ and $\boldsymbol{\ell}_2$. We can then distinguish three types of lattice according to the value of $\theta$: square lattice ($\theta = \pi/2$), rhombic lattice ($0 < \theta < \pi/2$, $\theta \neq \pi/3$) and hexagonal ($\theta = \pi/3$). After rotation, the generators of the planar lattices are given in table 1.1. Also shown are the generators of the *dual lattice* satisfying $\hat{\boldsymbol{\ell}}_i . \boldsymbol{\ell}_j = \delta_{i,j}$ with $|\hat{\boldsymbol{\ell}}_i| = 1$.



$D_6$ $\qquad\qquad\qquad\qquad$ $D_4$ $\qquad\qquad\qquad\qquad$ $D_2$
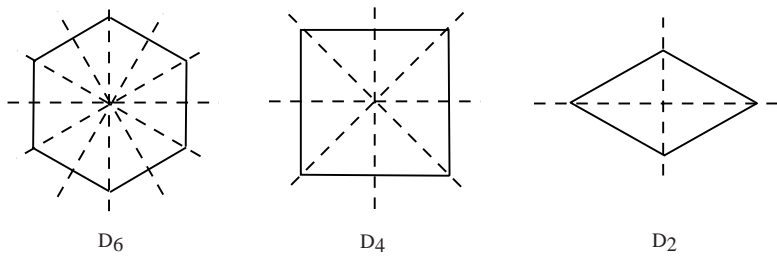
**Figure 1.16.** Holohedries of the plane

Imposing double periodicity means that the original Euclidean symmetry group is restricted to the symmetry group $\Gamma_{\mathcal{L}}$ of the lattice $\mathcal{L}$. In particular, there are only a finite number of shift-twists and reflections to consider for each lattice (modulo an arbitrary rotation of the whole plane), which correspond to the so-called holohedries of the plane, see figure 1.16. Consequently the corresponding space of marginally stable modes is now finite-dimensional—we can only rotate eigenfunctions through a finite set of angles (for example, multiples of $\pi/2$ for the square lattice and multiples of $\pi/3$ for the hexagonal lattice). The marginally stable modes for each of the lattices are given in table 1.2.

**Table 1.2.** Eigenmodes corresponding to shortest dual wave vectors $\mathbf{k}_i = q_c \hat{\boldsymbol{\ell}}_i$. Here $u(\phi) = \cos(2\phi)$ for even modes and $u(\phi) = \sin(2\phi)$ for odd modes.

| Lattice | $a(\mathbf{r}, \phi)$ |
|---------|------------------------|
| Square | $c_1 u(\phi) e^{i\mathbf{k}_1 \cdot \mathbf{r}} + c_2 u(\phi - \frac{\pi}{2}) e^{i\mathbf{k}_2 \cdot \mathbf{r}} + c.c.$ |
| Hexagonal | $c_1 u(\phi) e^{i\mathbf{k}_1 \cdot \mathbf{r}} + c_2 u(\phi - \frac{2\pi}{3}) e^{i\mathbf{k}_2 \cdot \mathbf{r}} + c_3 u(\phi + \frac{2\pi}{3}) e^{-i(\mathbf{k}_1 + \mathbf{k}_2) \cdot \mathbf{r}} + c.c.$ |
| Rhombic | $c_1 u(\phi) e^{i\mathbf{k}_1 \cdot \mathbf{r}} + c_2 u(\phi - \eta) e^{i\mathbf{k}_2 \cdot \mathbf{r}} + c.c.$ |

### 1.6.3   Selection and stability of patterns

It remains to determine the amplitudes $c_n$ of the doubly-periodic solutions that bifurcate from the homogeneous state (see table 1.2). We proceed by applying the perturbation method of § 1.5.1 to the amplitude equation (1.52). First, introduce a small parameter $\xi$ determining the distance from the point of marginal stability according to $\Delta\mu - \Delta\mu_c = \xi^2$ with $\Delta\mu_c = -\beta G_-(q_-)$ ($\Delta\mu_c = -\beta G_+(q_+)$) if odd (even) modes are marginally stable. Note that the parameter $\xi$ is independent of the coupling parameter $\varepsilon$. Also introduce a second slow time-scale $\hat{\tau} = \xi^2 \tau$. Next substitute the series expansion

$$z(\mathbf{r}, \hat{\tau}) = \xi z^{(1)}(\mathbf{r}, \hat{\tau}) + \xi^2 z^{(2)}(\mathbf{r}, \hat{\tau}) + \xi^3 z^{(3)}(\mathbf{r}, \hat{\tau}) + \dots \tag{1.80}$$

into equation (1.52) and collect terms with equal powers of $\xi$. This generates a hierarchy of equations of the form (up to $\mathcal{O}(\xi^3)$)

$$\mathcal{M}z^{(1)} = 0 \tag{1.81}$$

$$\mathcal{M}z^{(2)} = 0 \tag{1.82}$$

$$\mathcal{M}z^{(3)} = z^{(1)} \left[ 1 - A|z^{(1)}|^2 \right] - \frac{\mathrm{d}z^{(1)}}{\mathrm{d}\hat{\tau}} \tag{1.83}$$

where for any complex function $z$

$$\mathcal{M}z = -\Delta\mu_c z - \beta \int_0^\pi w_{lat} \circ \left[ z + \bar{z}\mathrm{e}^{-4i\phi} \right] \frac{d\phi}{\pi} \tag{1.84}$$

The first equation in the hierarchy has solutions of the form

$$z^{(1)}(\mathbf{r}, \hat{\tau}) = \Gamma \sum_{n=1}^N \mathrm{e}^{-2i\varphi_n} \left[ c_n(\hat{\tau})\mathrm{e}^{i\mathbf{k}_n \cdot \mathbf{r}} + \bar{c}_n(\hat{\tau})\mathrm{e}^{-i\mathbf{k}_n \cdot \mathbf{r}} \right] \tag{1.85}$$

where $\Gamma = 1$ for even $(+)$ modes and $\Gamma = i$ for odd $(-)$ modes (see equations (1.66) and (1.67)). Here $N = 2$ for the square or rhombic lattice and $N = 3$ for the hexagonal lattice. Also $\mathbf{k}_n = q_c\hat{\boldsymbol{\ell}}_n$ for $n = 1, 2$ and $\mathbf{k}_3 = -\mathbf{k}_1 - \mathbf{k}_2$. A dynamical equation for the amplitudes $c_n(\tau)$ can then be obtained as a solvability condition for the third-order equation (1.83). Define the inner product of two arbitrary doubly-periodic functions $f(\mathbf{r})$ and $g(\mathbf{r})$ by

$$\langle f|g \rangle = \int_\Lambda \bar{f}(\mathbf{r})g(\mathbf{r})d\mathbf{r} \tag{1.86}$$

where $\Lambda$ is a fundamental domain of the periodically tiled plane (whose area is normalized to unity). Taking the inner product of the left-hand side of equation (1.83) with $\tilde{f}_n(\mathbf{r}) = \mathrm{e}^{i\mathbf{k}_n \cdot \mathbf{r}}$ leads to the following solvability condition

$$\langle \tilde{f}_n | \mathrm{e}^{2i\varphi_n} \mathcal{M}z^{(3)} + \Gamma^2 \mathrm{e}^{-2i\varphi_n} \overline{\mathcal{M}z^{(3)}} \rangle = 0 \tag{1.87}$$

The factor $\Gamma^2 = \pm 1$ ensures that the appropriate marginal stability condition $\lambda_{\pm} = 0$ is satisfied by equation (1.71). Finally, we substitute for $\mathcal{M}z^{(3)}$ using the right-hand side of equation (1.83) to obtain an amplitude equation for $c_n$, which turns out to be identical for both odd and even solutions:

$$\frac{dc_n}{d\hat{\tau}} = c_n \left[ 1 - \gamma(0)|c_1|^2 - 2 \sum_{p \neq n} \gamma(\varphi_n - \varphi_p)|c_p|^2 \right] \qquad (1.88)$$

where

$$\gamma(\varphi) = [2 + \cos(4\varphi)]A \qquad (1.89)$$

We consider solutions of these amplitude equations for each of the basic lattices.

*Square or rhombic lattice*   First, consider planforms corresponding to a bimodal structure of the square or rhombic type ($N = 2$). That is, take $\mathbf{k}_1 = q_c(1,0)$ and $\mathbf{k}_2 = q_c(\cos(\theta), \sin(\theta))$, with $\theta = \pi/2$ for the square lattice and $0 < \theta < \pi/2$, $\theta \neq \pi/3$ for a rhombic lattice. The amplitudes evolve according to a pair of equations of the form

$$\frac{dc_1}{d\hat{\tau}} = c_1 \left[ 1 - \gamma(0)|c_1|^2 - 2\gamma(\theta)|c_2|^2 \right] \qquad (1.90)$$

$$\frac{dc_2}{d\hat{\tau}} = c_2 \left[ 1 - \gamma(0)|c_2|^2 - 2\gamma(\theta)|c_1|^2 \right] \qquad (1.91)$$

Since $\gamma(\theta) > 0$, three types of steady state are possible.

(i)   The homogeneous state: $c_1 = c_2 = 0$.
(ii)  Rolls: $c_1 = \sqrt{1/\gamma(0)}e^{i\psi_1}, c_2 = 0$ or $c_1 = 0, c_2 = \sqrt{1/\gamma(0)}e^{i\psi_2}$.
(iii) Squares or rhombics: $c_n = \sqrt{1/[\gamma(0) + 2\gamma(\theta)]}e^{i\psi_n}$, $n = 1, 2$.

for arbitrary phases $\psi_1, \psi_2$. A standard linear stability analysis shows that if $2\gamma(\theta) > \gamma(0)$ then rolls are stable whereas the square or rhombic patterns are unstable. The opposite holds if $2\gamma(\theta) < \gamma(0)$. Note that here stability is defined with respect to perturbations with the same lattice structure. Using equation (1.89) we deduce that in the case of a rhombic lattice of angle $\theta \neq \pi/2$, rolls are stable if $\cos(4\theta) > -1/2$ whereas $\theta$–rhombics are stable if $\cos(4\theta) < -1/2$, that is, if $\pi/6 < \theta < \pi/3$; rolls are stable and square patterns unstable on a square lattice.

*Hexagonal lattice*   Next consider planforms on a hexagonal lattice with $N = 3$, $\varphi_1 = 0$, $\varphi_2 = 2\pi/3$, $\varphi_3 = -2\pi/3$. The cubic amplitude equations take the form

$$\frac{dc_n}{d\hat{\tau}} = c_n \left[ 1 - \gamma(0)|c_n|^2 - 2\gamma(2\pi/3)(|c_{n+1}|^2 + |c_{n-1}|^2) \right] \qquad (1.92)$$

**Table 1.3.** Even and odd planforms for hexagonal lattice

| Even Planform | $(c_1, c_2, c_3)$ | Odd Planform | $(c_1, c_2, c_3)$ |
|---|---|---|---|
| 0-hexagon | $(1, 1, 1)$ | hexagon | $(1, 1, 1)$ |
| $\pi$-hexagon | $(1, 1, -1)$ | triangle | $(i, i, i)$ |
| roll | $(1, 0, 0)$ | roll | $(1, 0, 0)$ |
| | | patchwork quilt | $(0, 1, 1)$ |

where $n = 1, 2, 3 \mod 3$. Unfortunately, equation (1.92) is not sufficient to determine the selection and stability of the steady-state solutions bifurcating from the homogeneous state. One has to carry out an *unfolding* of the amplitude equation that includes higher-order terms (quartic and quintic) in $z, \bar{z}$. One could calculate this explicitly by carrying out a double expansion in the parameters $\varepsilon$ and $\xi$, which is equivalent to the perturbation approach used by [11]. In addition to generating higher-order terms, one finds that there is an $\mathcal{O}(\varepsilon)$ contribution to the coefficients $\gamma(\varphi)$ such that $2\gamma(2\pi/3) - \gamma(0) = \mathcal{O}(\varepsilon)$ and, in the case of even planforms, an $\mathcal{O}(\varepsilon)$ contribution to the right-hand side of equation (1.92) of the form $\eta \bar{c}_{n-1} \bar{c}_{n+1}$.
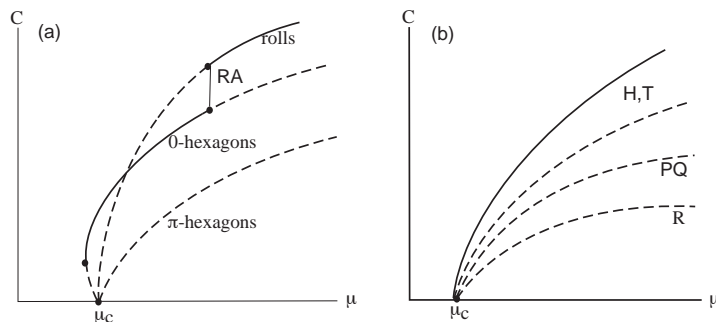


**Figure 1.17.** Bifurcation diagram showing the variation of the amplitude $C$ with the parameter $\mu$ for patterns on a hexagonal lattice. Solid and dashed curves indicate stable and unstable solutions respectively. *(a) Even patterns*: Stable hexagonal patterns are the first to appear (subcritically) beyond the bifurcation point. Subsequently the stable hexagonal branch exchanges stability with an unstable branch of roll patterns due to a secondary bifurcation that generates rectangular patterns $RA$. Higher–order terms in the amplitude equation are needed to determine its stability. *(b) Odd patterns*: Either hexagons (H) or triangles (T) are stable (depending on higher–order terms in the amplitude equation) whereas patchwork quilts (PQ) and rolls (R) are unstable. Secondary bifurcations (not shown) may arise from higher–order terms.

Considerable information about the bifurcating solutions can be obtained using group theoretic methods. First, one can use an important result from bifurcation theory in the presence of symmetries, namely, the *equivariant branching lemma* [29]:when a symmetric dynamical system goes unstable, new solutions emerge that (generically) have symmetries corresponding to the axial subgroups of the underlying symmetry group. A subgroup $\Sigma$ is *axial* if the dimension of the space of solutions that are fixed by $\Sigma$ is equal to one. Thus one can classify the bifurcating solutions by finding the axial subgroups of the symmetry group of the lattice (up to conjugacy). This has been carried out elsewhere for the particular shift-twist action of the Euclidean group described at the end of § 1.3 [11, 12]. The results are listed in table 1.3.

It can be seen that major differences emerge between the even and odd cases. Second, symmetry arguments can be used to determine the general
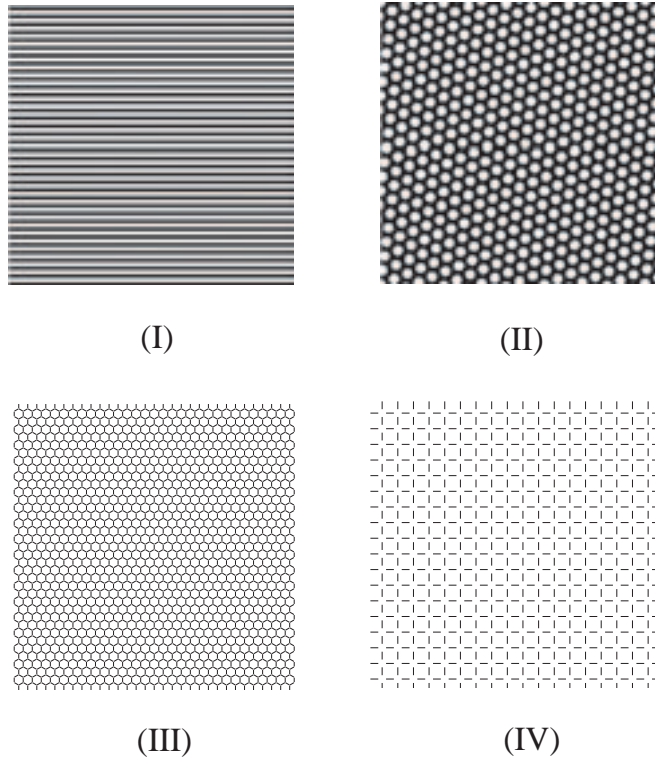


(I)  (II)

(III)  (IV)

**Figure 1.18.** V1 planforms. (I) Non-contoured roll (II) Non-contoured hexagon (III) Even contoured hexagon (IV) Even contoured square

form of higher-order contributions to the amplitude equation (1.92) and
this leads to the bifurcation diagrams shown in figure 1.17 [11, 12]. It
turns out that stability depends crucially on the sign of the $\mathcal{O}(\varepsilon)$ coeffi-
cient $2\gamma(2\pi/3) - \gamma(0)$, which is assumed to be positive in figure 1.17. The
subcritical nature of the bifurcation to hexagonal patterns in the case of
even patterns is a consequence of an additional quadratic term appearing
on the right-hand side of (1.92).

### 1.6.4 From cortical patterns to geometric visual hallucinations

We have now identified the stable planforms that are generated as primary
bifurcations from a homogeneous, low activity state of the continuum model
(1.24). These planforms consist of certain linear combinations of the roll
patterns shown in figure 1.15 and can thus be classified into non-contoured
($m = 0$) and contoured ($m = 1$ even or odd) patterns. Given a particular
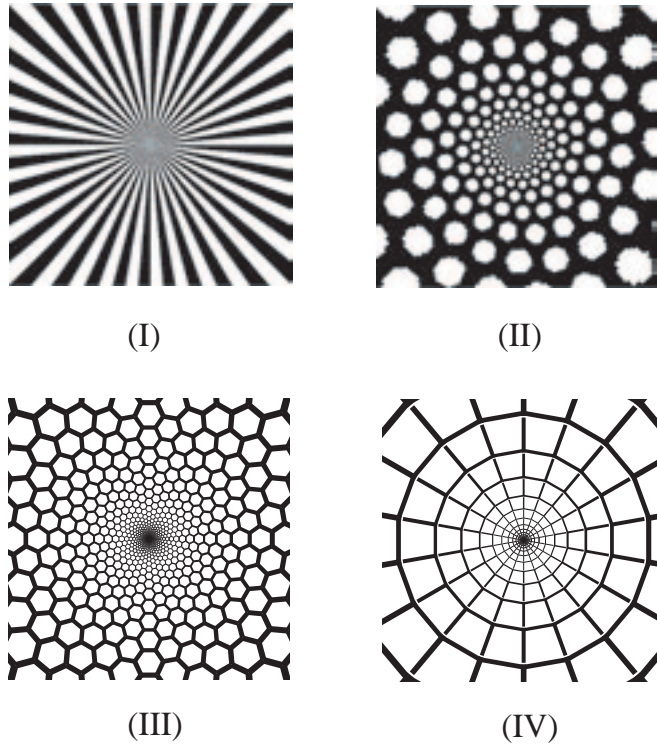activity state in cortex, we can infer what the corresponding image in visual



(I)

(II)

(III)

(IV)

**Figure 1.19.** Visual field images of V1 planforms shown in figure 1.18

coordinates is like by applying the inverse of the retino-cortical map shown in figure 1.2. (In the case of contoured patterns, one actually has to specify the associated tangent map as detailed in [11]). Some examples of stable V1 planforms are presented in figure 1.18 and the associated visual images are presented in figure 1.19. It will be seen that the two non-contoured planforms correspond to the type (I) and (II) Kluver form constants, as originally proposed by Ermentrout and Cowan [22], whereas the two contoured planforms reproduce the type (III) and (IV) form constants (see figure 1.10).

### 1.6.5   Oscillating patterns

It is also possible for the cortical model to spontaneously form oscillating patterns. This will occur if, in the absence of any lateral connections, each hypercolumn undergoes a Hopf bifurcation to a time–periodic tuning curve along the lines described in § 1.5.3. (It is not possible for the lateral connections to induce oscillations when the individual hypercolumns exhibit stationary tuning curves. This is a consequence of the fact that the lateral connections are modulatory and originate only from excitatory neurons). Linearizing equations (1.62) and (1.63) about the zero state $z_R = z_L = 0$ (assuming zero inputs from the LGN) gives

$$\frac{\partial z_L(\mathbf{r}, \tau)}{\partial \tau} = \Delta\mu(1 + i\Omega_0)z_L(\mathbf{r}, \tau)$$
$$+ \beta \int_0^\pi w_{lat} \circ \left[ z_L(\mathbf{r}, \tau) + z_R(\mathbf{r}, \tau)\mathrm{e}^{4i\phi} \right] \frac{d\phi}{\pi} \qquad (1.93)$$

$$\frac{\partial z_R(\mathbf{r}, \tau)}{\partial \tau} = \Delta\mu(1 + i\Omega_0)z_R(\mathbf{r}, \tau)$$
$$+ \beta \int_0^\pi w_{lat} \circ \left[ z_R(\mathbf{r}, \tau) + z_L(\mathbf{r}, \tau)\mathrm{e}^{-4i\phi} \right] \frac{d\phi}{\pi} \qquad (1.94)$$

Equation (1.93) and (1.94) have solutions of the form

$$z_L(\mathbf{r}, \tau) = u\mathrm{e}^{\lambda\tau}\mathrm{e}^{2i\varphi}\mathrm{e}^{i\mathbf{k}.\mathbf{r}}, \quad z_R(\mathbf{r}, \tau) = v\mathrm{e}^{\lambda\tau}\mathrm{e}^{-2i\varphi}\mathrm{e}^{i\mathbf{k}.\mathbf{r}} \qquad (1.95)$$

where $\mathbf{k} = q(\cos(\varphi), \sin(\varphi))$ and $\lambda$ is determined by the eigenvalue equation

$$[\lambda - \Delta\mu(1 + i\Omega_0)] \begin{pmatrix} u \\ v \end{pmatrix} = \beta \begin{pmatrix} G_0(q) & \chi G_2(q) \\ \chi G_2(q) & G_0(q) \end{pmatrix} \begin{pmatrix} u \\ v \end{pmatrix} \quad (1.96)$$

with $G_n(q)$ given by equation (1.73). Equation (1.96) has solutions of the form

$$\lambda_\pm = \Delta\mu(1 + i\Omega_0) + \beta G_\pm(q), \quad v = \pm u \qquad (1.97)$$

for $G_{\pm}(q)$ defined by equation (1.72).

Hence, as in the case of stationary patterns, either odd or even time-periodic patterns will bifurcate from the homogeneous state depending on the degree of spread in the lateral connections. Close to the bifurcation point these patterns are approximated by the eigenfunctions of the linear theory according to

$$a(\mathbf{r}, \phi, t) = \sum_{n=1}^{N} \cos(2[\phi - \varphi_n]) \left[ c_n e^{i(\Omega t + \mathbf{k}_n \cdot \mathbf{r})} + d_n e^{i(\Omega t - \mathbf{k}_n \cdot \mathbf{r})} + c.c \right]$$

(1.98)

with $\mathbf{k}_n = q_+(\cos \varphi_n, \sin \varphi_n)$ for even solutions and

$$a(\mathbf{r}, \phi, t) = \sum_{n=1}^{N} \sin(2[\phi - \varphi_n]) \left[ c_n e^{i(\Omega t + \mathbf{k}_n \cdot \mathbf{r})} + d_n e^{i(\Omega t - \mathbf{k}_n \cdot \mathbf{r})} + c.c. \right]$$

(1.99)

with $\mathbf{k}_n = q_-(\cos \varphi_n, \sin \varphi_n)$ for odd solutions, and where $\Omega = \Omega_0(1 + \varepsilon \Delta \mu)$. These should be compared with the corresponding solutions (1.75) and (1.77) of the stationary case. An immediate consequence of our analysis is that the oscillating patterns form standing waves within a single hypercolumn, that is, with respect to the orientation label $\phi$. However, it is possible for travelling waves to propagate across V1 if there exist solutions for which $c_n \neq 0$, $d_n = 0$ or $c_n = 0$, $d_n \neq 0$. In order to investigate this possibility, we carry out a perturbation analysis of equations 1.62 and (1.63) along the lines of § 1.6.3 (after the restriction to doubly periodic solutions).

First, introduce a second slow time variable $\hat{\tau} = \xi^2 \tau$ where $\xi^2 = \Delta \mu - \Delta \mu_c$ and take $z_{L,R} = z_{L,R}(\mathbf{r}, \tau, \hat{\tau})$. Next, substitute into equations (1.62) and (1.63) the series expansions

$$z_{L,R} = \xi z_{L,R}^{(1)} + \xi^2 z_{L,R}^{(2)} + \xi^3 z_{L,R}^{(3)} + \dots$$

(1.100)

and collect terms with equal powers of $\xi$. This generates a hierarchy of equations of the form (up to $\mathcal{O}(\xi^3)$)

$$\left[ \mathcal{M}_\tau \mathbf{z}^{(p)} \right]_L = 0, \quad \left[ \mathcal{M}_\tau \mathbf{z}^{(p)} \right]_R = 0$$

(1.101)

for $p = 1, 2$ and

$$\left[ \mathcal{M}_\tau \mathbf{z}^{(3)} \right]_L = (1 + i\Omega_0) z_L^{(1)} \left[ 1 - A|z_L^{(1)}|^2 - 2A|z_R^{(1)}|^2 \right] - \frac{\partial z_L^{(1)}}{\partial \hat{\tau}} \quad (1.102)$$

$$\left[ \mathcal{M}_\tau \mathbf{z}^{(3)} \right]_R = (1 + i\Omega_0) z_R^{(1)} \left[ 1 - A|z_R^{(1)}|^2 - 2A|z_L^{(1)}|^2 \right] - \frac{\partial z_R^{(1)}}{\partial \hat{\tau}} \quad (1.103)$$

where for any $\mathbf{z} = (z_L, z_R)$

$$[\mathcal{M}_\tau \mathbf{z}]_L = \frac{\partial z_L}{\partial \tau} - (1 + i\Omega_0)\Delta\mu_c z_L - \beta \int_0^\pi w_{lat} \circ \left[z_L + z_R \mathrm{e}^{+4i\phi}\right] \frac{d\phi}{\pi}$$

(1.104)

$$[\mathcal{M}_\tau \mathbf{z}]_R = \frac{\partial z_L}{\partial \tau} - (1 + i\Omega_0)\Delta\mu_c z_R - \beta \int_0^\pi w_{lat} \circ \left[z_R + z_L \mathrm{e}^{-4i\phi}\right] \frac{d\phi}{\pi}$$

(1.105)

The first equation in the hierarchy has solutions of the form

$$z_L^{(1)}(\mathbf{r}, \tau, \hat{\tau}) = \mathrm{e}^{i\delta\Omega\tau} \sum_{n=1}^N \mathrm{e}^{2i\varphi_n} \left[c_n(\hat{\tau})\mathrm{e}^{i\mathbf{k}_n \cdot \mathbf{r}} + d_n(\hat{\tau})\mathrm{e}^{-i\mathbf{k}_n \cdot \mathbf{r}}\right] \quad (1.106)$$

$$z_R^{(1)}(\mathbf{r}, \tau, \hat{\tau}) = \Gamma\mathrm{e}^{i\delta\Omega\tau} \sum_{n=1}^N \mathrm{e}^{-2i\varphi_n} \left[c_n(\hat{\tau})\mathrm{e}^{i\mathbf{k}_n \cdot \mathbf{r}} + d_n(\hat{\tau})\mathrm{e}^{-i\mathbf{k}_n \cdot \mathbf{r}}\right] \quad (1.107)$$

where $\Gamma = 1$ for even modes and $\Gamma = -1$ for odd modes (see equations (1.95) and (1.97)), and $\delta\Omega = \Omega_0\Delta\mu_c$. As in the stationary case we restrict ourselves to doubly periodic solutions with $N = 2$ for the square or rhombic lattice and $N = 3$ for the hexagonal lattice. A dynamical equation for the complex amplitudes $c_n(\hat{\tau})$ and $d_n(\hat{\tau})$ can be obtained as a solvability condition for the third-order equations (1.102) and (1.103). Define the inner product of two arbitrary doubly-periodic vectors $\mathbf{f}(\mathbf{r}, \tau) = (f_L(\mathbf{r}, \tau), f_R(\mathbf{r}, \tau))$ and $\mathbf{g}(\mathbf{r}, \tau) = (g_L(\mathbf{r}, \tau), g_R(\mathbf{r}, \tau))$ by

$$\langle\mathbf{f}|\mathbf{g}\rangle = \lim_{T\to\infty} \frac{1}{T} \int_{-T/2}^{T/2} \int_\Lambda \left[f_L(\mathbf{r}, \tau)g_L(\mathbf{r}, \tau) + f_R(\mathbf{r}, \tau)g_R(\mathbf{r}, \tau)\right] d\mathbf{r}d\tau$$

(1.108)

where $\Lambda$ is a fundamental domain of the periodically tiled plane (whose area is normalized to unity). Taking the inner product of the left-hand side of equation (1.83) with the vectors $\tilde{\mathbf{f}}_n(\mathbf{r}, \tau) = \mathrm{e}^{i\mathbf{k}_n \cdot \mathbf{r}}\mathrm{e}^{i\delta\Omega\tau}(\mathrm{e}^{2i\varphi_n}, \Gamma\mathrm{e}^{-2i\varphi_n})$ and $\tilde{\mathbf{g}}_n(\mathbf{r}, \tau) = \mathrm{e}^{-i\mathbf{k}_n \cdot \mathbf{r}}\mathrm{e}^{i\delta\Omega\tau}(\mathrm{e}^{2i\varphi_n}, \Gamma\mathrm{e}^{-2i\varphi_n})$ leads to the following pair of solvability conditions

$$\langle\tilde{\mathbf{f}}_n|\mathcal{M}_\tau\mathbf{z}^{(3)}\rangle = 0, \quad \langle\tilde{\mathbf{g}}_n|\mathcal{M}_\tau\mathbf{z}^{(3)}\rangle = 0, \tag{1.109}$$

Finally, we substitute for $\mathcal{M}_\tau\mathbf{z}^{(3)}$ using equations (1.102) and (1.103) to obtain amplitude equations for $c_n$ and $d_n$ (which at this level of approximation are the same for odd and even solutions):

$$\frac{dc_n}{d\hat{\tau}} = -4(1 + i\Omega_0)\bar{d}_n \sum_{p\neq n} \gamma(\varphi_n - \varphi_p)c_p d_p + (1 + i\Omega_0)c_n \tag{1.110}$$

$$\times \left[ 1 - 2\gamma(0)(|c_n|^2 + 2|d_n|^2) - 4\sum_{p\neq n} \gamma(\varphi_n - \varphi_p)(|c_p|^2 + |d_p|^2) \right]$$

$$\frac{\mathrm{d}d_n}{\mathrm{d}\hat{\tau}} = -4(1 + i\Omega_0)\bar{c}_n \sum_{p\neq n} \gamma(\varphi_n - \varphi_p)c_p d_p + (1 + i\Omega_0)d_n \qquad (1.111)$$

$$\times \left[ 1 - 2\gamma(0)(|d_n|^2 + 2|c_n|^2) - 4\sum_{p\neq n} \gamma(\varphi_n - \varphi_p)(|c_p|^2 + |d_p|^2) \right]$$

with $\gamma(\varphi)$ given by equation (1.89).

The analysis of the amplitude equations (1.110) and (1.111) is considerably more involved than for the corresponding stationary problem. We discuss only the square lattice here ($N = 2$) with $\mathbf{k}_1 = q_c(1,0)$ and $\mathbf{k}_2 = q_c(0,1)$, The four complex amplitudes $(c_1, c_2, d_1, d_2)$ evolve according to the set of equations of the form

$$\frac{\mathrm{d}c_1}{\mathrm{d}\hat{\tau}} = (1 + i\Omega_0)\left( c_1 \left[ 1 - \kappa(|c_1|^2 + 2|d_1|^2) - 2\kappa(|c_2|^2 + |d_2|^2) \right] - 2\kappa\bar{d}_1 c_2 d_2 \right)$$

$$(1.112)$$

$$\frac{\mathrm{d}c_2}{\mathrm{d}\hat{\tau}} = (1 + i\Omega_0)\left( c_2 \left[ 1 - \kappa(|c_2|^2 + 2|d_2|^2) - 2\kappa(|c_1|^2 + |d_1|^2) \right] - 2\kappa\bar{d}_2 c_1 d_1 \right)$$

$$(1.113)$$

$$\frac{\mathrm{d}d_1}{\mathrm{d}\hat{\tau}} = (1 + i\Omega_0)\left( d_1 \left[ 1 - \kappa(|c_1|^2 + 2|d_1|^2) - 2\kappa(|c_2|^2 + |d_2|^2) \right] - 2\kappa\bar{c}_1 c_2 d_2 \right)$$

$$(1.114)$$

$$\frac{\mathrm{d}d_2}{\mathrm{d}\hat{\tau}} = (1 + i\Omega_0)\left( d_2 \left[ 1 - \kappa(|c_2|^2 + 2|d_2|^2) - 2\kappa(|c_1|^2 + |d_1|^2) \right] - 2\kappa\bar{d}_2 c_1 d_1 \right)$$

$$(1.115)$$

where $\kappa = 6A$. These equations have the same structure as the cubic equations obtained for the standard Euclidean group action using group theoretic methods [51]. An identical set of equations has been obtained for oscillatory activity patterns in the Ermentrout-Cowan model [56]. It can be shown that there exist five possible classes of solution that can bifurcate from the homogeneous state. We list examples from each class:

(i) Travelling rolls (TR): $c_1 \neq 0, c_2 = d_1 = d_2 = 0$ with $|c_1|^2 = 1/\kappa$.
(ii) Travelling squares (TS): $c_1 = c_2 \neq 0, d_1 = d_2 = 0$ with $|c_1|^2 = 1/3\kappa$

(iii) Standing rolls (SR): $c_1 = d_1, c_2 = d_2 = 0$ with $|c_1|^2 = 1/3\kappa$
(iv) Standing squares (SS): $c_1 = d_1 = c_2 = d_2$ with $|c_1|^2 = 1/9\kappa$
(v) Alternating rolls (AR): $c_1 = -ic_2 = d_1 = -id_2$ with $|c_1|^2 = 1/5\kappa$

Up to arbitrary phase-shifts the corresponding planforms are

$(TR)$ $\quad a(\mathbf{r}, \phi, t) = |c_1| u(\phi) \cos(\Omega t + q_c x)$

$(TS)$ $\quad a(\mathbf{r}, \phi, t) = |c_1| \left[ u(\phi) \cos(\Omega t + q_c x) + u(\phi - \pi/2) \cos(\Omega t + q_c y) \right]$

$(SR)$ $\quad a(\mathbf{r}, \phi, t) = |c_1| u(\phi) \cos(\Omega t) \cos(q_c x)$

$(SS)$ $\quad a(\mathbf{r}, \phi, t) = |c_1| \cos(\Omega t) \left[ u(\phi) \cos(q_c x) + u(\phi - \pi/2) \cos(q_c y) \right]$

$(AR)$ $\quad a(\mathbf{r}, \phi, t) = |c_1| \left[ \cos(\Omega t) u(\phi) \cos(q_c x) + \sin(\Omega t) u(\phi - \pi/2) \cos(q_c y) \right]$

(In contrast to the more general case considered by [51], our particular system does not support standing cross-roll solutions of the form $c_1 = d_1, c_2 = d_2$ with $|c_1| \neq |c_2|$).

    Linear stability analysis shows that (to cubic order) the TR solution is stable, the AR solution is marginally stable and the other solutions are unstable [51, 56]. In order to resolve the degeneracy of the AR solution one would need to carry out a double expansion in the parameters $\xi, \varepsilon$ and include higher order terms in the amplitude equation. The situation is even more complicated in the case of the hexagonal lattice where such a double expansion is expected to yield additional contributions to equations (1.110) and (1.111). As in the stationary case, group theoretic methods can be used to determine generic aspects of the bifurcating solutions. First note that as with other Hopf bifurcation problems the amplitude equations have an extra phase-shift symmetry in time that was not in the original problem. This takes the form $\psi : (c_n, d_n) \to (e^{i\psi} c_n, e^{i\psi} d_n)$ for $n = 1, \ldots, N$ with $\psi \in \mathbf{S}^1$. Thus the full spatio-temporal symmetry is $\Gamma_{\mathcal{L}} \times \mathbf{S}^1$ for a given lattice $\mathcal{L}$. One can then appeal to the *equivariant Hopf theorem* [29] which guarantees the existence of primary bifurcating branches that have symmetries corresponding to the isotropy subgroups of $\Gamma_{\mathcal{L}} \times \mathbf{S}^1$ with two-dimensional fixed point subspaces. (In the case of a square lattice this generates the five solutions listed above). The isotropy subgroups for the standard Euclidean group action have been calculated elsewhere [46, 51, 20]. As in the stationary bifurcation problem, the isotropy subgroups of the shift-twist action may differ in a non-trivial way. This particular issue will be explored elsewhere.

## 1.7   Spatial frequency tuning and SO(3) symmetry

One of the simplifications of our large-scale cortical model has been to treat V1 as a continuum of interacting hypercolumns in which the internal structure of each hypercolumn is idealized as a ring of orientation selective cells. This reduction can be motivated in part by the fact that there exists

a physical ring of orientation domains around each pinwheel, as illustrated by the circle in figure 1.4. However, even if one restricts attention to the single eye case, there still exist two pinwheels per ocular dominance column. Moroever, the ring model does not take into account the fact that within each pinwheel region there is a broad distribution of orientation preferences so that the average orientation selectivity is weak. A fuller treatment of the two-dimensional structure of a hypercolumn can be carried out by incorporating another internal degree of freedom within the hypercolumn, which reflects the fact that cortical cells are also selective to the spatial frequency of a stimulus. (In the case of a grating stimulus, this would correspond to the inverse of the wavelength of the grating). Indeed, recent optical imaging data suggests that the two pinwheels per hypercolumn are associated with high and low spatial frequencies respectively [7, 36, 37]. Recently, we have proposed a generalization of the ring model that takes into account this structure by incorporating a second internal degree of freedom corresponding to (log) spatial frequency preference [15]. Here we show how this new model can be used to extend our theory of cortical pattern formation to include both orientation and spatial frequency preferences.

### 1.7.1   The spherical model of a hypercolumn

Each hypercolumn (when restricted to a single ocular dominance column) is now represented by a sphere with the two orientation singularities identified as the north and south poles respectively (see figure 1.20). Following recent optical imaging results [7, 36, 37], the singularities are assumed to correspond to the two extremes of (log) spatial frequency within the hypercolumn. In terms of spherical polar coordinates $(r, \theta, \varphi)$ with $r = 1$, $\theta \in [0, \pi)$ and $\varphi \in [0, 2\pi)$, we thus define the orientation preference $\phi$ and (log) spatial frequency $\nu$ according to

$$\nu = \nu_{min} + \frac{\theta}{\pi} \left[\nu_{max} - \nu_{min}\right], \quad \phi = \varphi/2 \qquad (1.116)$$

Note that we consider $\nu = \log p$ rather than spatial frequency $p$ as a cortical label. This is motivated by the observation that dilatations in visual field coordinates correspond to horizontal translations in cortex (see § 1.1). Using certain scaling arguments it can then be shown that all hypercolumns have approximately the same bandwidth in $\nu$ even though there is broadening with respect to lower spatial frequencies as one moves towards the periphery of the visual field [15].

It is important to emphasize that the sphere describes the network topology of the local weight distribution expressed in terms of the internal labels for orientation and spatial frequency. It is not, therefore, expected to match the actual spatial arrangement of cells within a hypercolumn. Given this spherical topology, the natural internal symmetry of a hypercolumn is
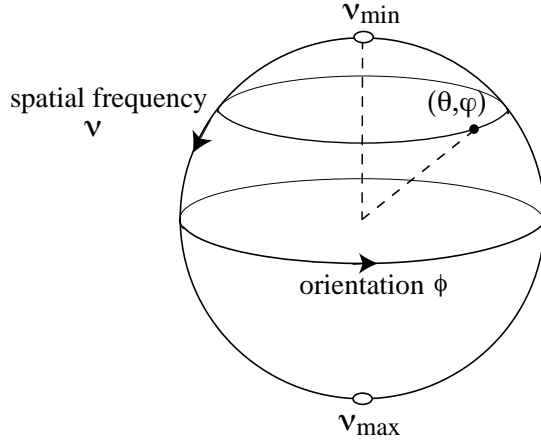
**Figure 1.20.** Spherical model of orientation and spatial frequency tuning

now **SO**(3) rather than **O**(2). In particular, the local weight distribution is assumed to be **SO**(3) invariant. Imposing such a symmetry is not just a mathematical convenience, but actually reflects the anatomical observation that the pattern of local interactions within a hypercolumn depends on cortical separation rather than feature separation [19]. When the weight distribution is expressed in terms of cortical co-ordinates, this naturally leads to Euclidean symmetry. However, we are describing the interactions in terms of cortical labels for orientation and spatial frequency. Hence, the natural measure of spatial separation is now in terms of geodesics or great circles on the sphere, and the group that preserves geodesic separation is **SO**(3).

Having introduced the spherical model of a single hypercolumn, it is straightforward to write down a generalization of our large-scale cortical model given by equation (1.19):

$$\frac{\partial a(\mathbf{r}, P, t)}{\partial t} = -a(\mathbf{r}, P, t) + \int w(P|P')\sigma[a(\mathbf{r}, P', t)]dP' \qquad (1.117)$$

$$+ \varepsilon \int w_{lat}(\mathbf{r}, P|\mathbf{r}', P')\sigma[a(\mathbf{r}', P', t)]d\mathbf{r}'dP' + h(\mathbf{r}, P, t)$$

where we have introduced the compact notation $P = \{\theta, \varphi\}$ and $dP = \sin\theta d\theta d\varphi$. (For ease of notation, we consider here a one-population model by identifying the states $a_E = a_I$. Note that such a state arose previously in case A of § 1.4). In equation (1.117), $w(P|P')$ denotes the distribution of local connections within a hypercolumn, whereas $w_{lat}(\mathbf{r}, P|\mathbf{r}', P')$ denotes the distribution of horizontal connections between the hypercolumns

at **r** and **r**′. In the following we focus on the spontaneous dynamical behaviour of the model by fixing $h(\mathbf{r}, P, t) = h_0$ such that $a(\mathbf{r}, P, t) = a_0$ is a homogeneous fixed point solution of equation (1.117).

An **SO**(3) invariant local weight distribution can be constructed in terms of spherical harmonics [15]:

$$w(\theta, \varphi | \theta', \varphi') = \mu \sum_{n=0}^{\infty} W_n \sum_{m=-n}^{n} \overline{Y_n^m}(\theta', \varphi') Y_n^m(\theta, \varphi) \qquad (1.118)$$

with $W_n$ real. The functions $Y_n^m(\theta, \varphi)$ constitute the angular part of the solutions of Laplace's equation in three dimensions, and thus form a complete orthonormal set. The orthogonality relation is

$$\int_0^{2\pi} \int_0^{\pi} \overline{Y_{n_1}^{m_1}}(\theta, \varphi) Y_{n_2}^{m_2}(\theta, \varphi) \sin\theta \, d\theta \, d\varphi = \delta_{n_1, n_2} \delta_{m_1, m_2} \qquad (1.119)$$

The spherical harmonics are given explicitly by

$$Y_n^m(\theta, \varphi) = \mathcal{P}_n^m(\cos\theta) e^{im\varphi} \qquad (1.120)$$

with

$$\mathcal{P}_n^m(\cos\theta) = (-1)^m \sqrt{\frac{2n+1}{4\pi} \frac{(n-m)!}{(n+m)!}} P_n^m(\cos\theta) \qquad (1.121)$$

for $n \geq 0$ and $-n \leq m \leq n$, where $P_n^m(\cos\theta)$ is an associated Legendre function. The lowest order spherical harmonics are listed below

$$Y_0^0(\theta, \varphi) = \frac{1}{\sqrt{4\pi}} \qquad (1.122)$$

$$Y_1^0(\theta, \varphi) = \sqrt{\frac{3}{4\pi}} \cos\theta, \quad Y_1^{\pm}(\theta, \varphi) = \mp\sqrt{\frac{3}{8\pi}} \sin\theta \, e^{\pm i\varphi} \qquad (1.123)$$

In figure 1.21 we show a contour plot of the $SO(3)$ invariant weight distribution for the particular case $W_0 = 1$, $W_1 = 3$, and $W_n = 0$ for $n \geq 2$. The contour plot represents the distribution joining neurons with the same spatial frequency (same latitude on the sphere). It can be seen that away from the pinwheels (poles of the sphere), cells with similar orientation excite each other whereas those with dissimilar orientation inhibit each other. This is the standard interaction assumption of the ring model (see § 1.4). On the other hand, around the pinwheels, all orientations uniformly excite, which is consistent with the experimental observation that local interactions depend on cortical separation [19]. That is, although the cells around a pinwheel can differ greatly in their orientation preference, they are physically close together within the hypercolumn.

How does the anisotropy in the lateral connections manifest itself when spatial frequency is taken into account, so that the internal symmetry is
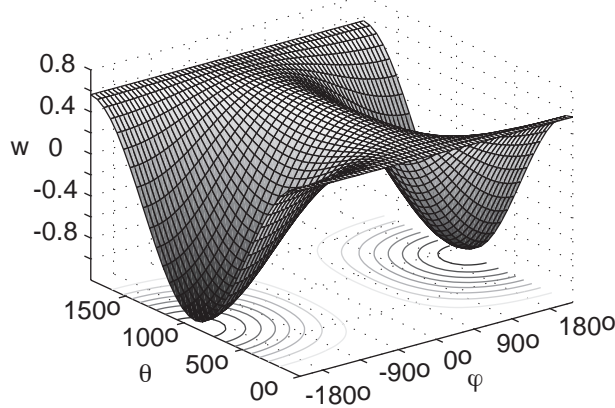
**Figure 1.21.** Plot of $w(\theta, \varphi | \theta', \varphi')$ given by the $SO(3)$ invariant weight distribution (1.118) with $W_0 = 1$, $W_1 = 3$ and $W_n = 0$ for $n \geq 2$. Since $w$ only depends on the difference $\varphi - \varphi'$, we set $\varphi' = 0$ and plot $w$ as a function of $\theta$ and $\varphi$ for $\theta' = \theta$.

**SO**(3) rather than **O**(2)? The first point to make is that, unlike **O**(2), **SO**(3) does not have a faithful representation in $\mathbf{R}^2$. Nevertheless, it is possible to generalize equation (1.22) so that the weights are invariant with respect to the action of $\mathbf{R}^2 \dot{+} O(2) = \mathbf{E}(2)$ on $\{\mathbf{r}, \theta, \varphi\}$. That is, we consider a lateral weight distribution of the form

$$w_{lat}(\mathbf{r}, P | \mathbf{r}', P') = \varepsilon J(T_{-\varphi/2}(\mathbf{r} - \mathbf{r}')) \frac{1}{\sin \theta'} \delta(\theta - \theta') \delta(\varphi - \varphi') \qquad (1.124)$$

with $J(\mathbf{r})$ defined by equation (1.23) and $\varepsilon < 0$ (inhibitory lateral interactions). Such a distribution links neurons with the same orientation and spatial frequency label, with the function $p(\eta)$ again determining the degree of spatial spread (anisotropy) in the pattern of connections relative to the direction of their common orientation preference. An elegant feature of the spherical model is that it naturally incorporates the fact that, at the population level, there is less selectivity for orientation near pinwheels. In other words, any solution $a(\mathbf{r}, \theta, \varphi)$ expanded in terms of spherical harmonics is independent of $\varphi$ at $\theta = 0, \pi$. This constrains the allowed structure of the spread function $p(\eta)$, in the sense that the horizontal weight distribution (1.124) has to be isotropic at the pinwheels. This follows from equations (1.124) and (1.23), which show that

$$\int w_{lat}(\mathbf{r}, P | \mathbf{r}', P') a(\mathbf{r}', P') dP'$$

$$= \int_{-\infty}^{\infty} g(s) \int_{-\pi/2}^{\pi/2} p(\eta)a(\mathbf{r} + s\mathbf{r}_{\varphi/2+\eta}, P)d\eta ds \qquad (1.125)$$

It is clear that the right-hand of this equation will be independent of $\varphi$ at $\theta = 0, \pi$ if and only if $p(\eta) = 1/\pi$ at the pinwheels. In order to incorporate the known anisotropy away from the pinwheels, we conclude that the spread function has to be $\theta$-dependent, $p = p(\eta|\theta)$. An example of a spread function that smoothly interpolates between isotropic connections at the pinwheels (high and low spatial frequencies) and strong anisotropy in the linear zones (intermediate spatial frequencies) with degree of spread $\eta_0$ is

$$p(\eta|\theta) = \frac{\cos^2 \theta}{\pi} + \frac{1}{2\eta_0}\Theta(\eta_0 - |\eta|)\sin^2 \theta \qquad (1.126)$$

The anisotropic weight distribution (1.124) is invariant under the following action of $\mathbf{R}^2 \dot{+} O(2) = \mathbf{E}(2)$ on $\{\mathbf{r}, \theta, \varphi\}$:

$$\begin{aligned}
\mathbf{s} \cdot (\mathbf{r}, \theta, \varphi) &= (\mathbf{r} + \mathbf{s}, \theta, \varphi) \quad \mathbf{s} \in \mathbf{R}^2 \\
\xi \cdot (\mathbf{r}, \theta, \varphi) &= (T_\xi \mathbf{r}, \theta, \varphi + \xi) \quad \xi \in S^1 \\
\kappa \cdot (\mathbf{r}, \theta, \varphi) &= (\kappa \mathbf{r}, \theta, -\varphi)
\end{aligned} \qquad (1.127)$$

where $\kappa$ is the reflection $(x_1, x_2) \mapsto (x_1, -x_2)$.

### 1.7.2 Cortical patterns and spatial frequency tuning

A theory of spontaneous pattern formation in the coupled spherical model (1.117) can be developed along similar lines to that of the coupled ring model (1.24). Now each isolated hypercolumn generates a *tuning surface* for orientation and spatial frequency through spontaneous **SO**(3) symmetry breaking. The peak of this surface can be locked to a weakly biased stimulus from the LGN. Moreover, lateral interactions induce correlations between the tuning surfaces across the cortex leading to spatially periodic patterns of activity, which are consistent with the hallucinatory images presented in § 1.6.4. Rather than presenting the full nonlinear analysis here, we restrict ourselves to studying the linear eigenmodes that are excited when a homogeneous fixed point of the network becomes unstable.

First, we linearize equation (1.117) about the fixed point solution $a(\mathbf{r}, \theta, \varphi, t) = a_0$. Setting $a(\mathbf{r}, \theta, \varphi, t) = a_0 + e^{\lambda t}u(\theta, \varphi)e^{i\mathbf{k}\cdot\mathbf{r}}$ generates the eigenvalue equation

$$\lambda u(P) = -u(P) + \mu \int w(P|P')u(P')dP' + \varepsilon \widetilde{J}(T_{\varphi/2}\mathbf{k})u(P) \qquad (1.128)$$

where $\widetilde{J}(\mathbf{k})$ is the Fourier transform of $J(\mathbf{r})$ and $\mathbf{k} = q(\cos\zeta, \sin\zeta)$. Expanding $u(\theta, \varphi)$ in terms of spherical harmonics

$$u(\theta, \varphi) = \sum_{n \in \mathbf{Z}} \sum_{m=-n}^{n} e^{-im\zeta} A_{nm}Y_n^m(\theta, \varphi) \qquad (1.129)$$

leads to the matrix eigenvalue equation

$$[\lambda + 1 - \mu W_n] A_{nm} = \varepsilon \sum_{n' \in \mathbf{Z}} \sum_{m'=-n'}^{n'} J_{nm,n'm'}(q) A_{n'm'} \qquad (1.130)$$

with

$$J_{nm,n'm'}(q) = \int_0^{2\pi} \int_0^{\pi} \overline{Y_n^m}(\theta, \varphi) Y_{n'}^{m'}(\theta, \varphi) \qquad (1.131)$$

$$\times \left[ \int_{\pi/2}^{\pi/2} p(\eta|\theta) \int_0^{\infty} g(s) \cos(sq \cos[\varphi/2 + \eta]) d\eta ds \right] \sin \theta d\theta d\varphi$$

We have included an additional phase-factor $\mathrm{e}^{-im\zeta}$ in equation (1.129) that simplifies the matrix equation (1.130) by eliminating any dependence on the direction $\zeta$ of the wavevector $\mathbf{k}$. Such a phase factor is equivalent to shifting $\varphi$, since $\mathrm{e}^{-im\zeta} Y_n^m(\theta, \varphi) = Y_n^m(\theta, \varphi - \zeta)$.

The matrix elements $J_{nm,n'm'}(q)$ are evaluated by substituting the explicit expression (1.120) for the spherical harmonics into equation (1.131):

$$J_{nm,n'm'}(q) = 2\pi G_{m-m'}(q) \Gamma_{nm,n'm'} \qquad (1.132)$$

where $G_m(q)$ satisfies equation (1.73) and

$$\Gamma_{nm,n'm'} = \int_0^{\pi} \mathcal{P}_n^m(\cos \theta) \mathcal{P}_{n'}^{m'}(\cos \theta) \left[ \int_{-\pi/2}^{\pi/2} p(\eta|\theta) \mathrm{e}^{2i(m-m')\eta} d\eta \right] \sin \theta d\theta$$

$$(1.133)$$

For the spread function (1.126) we have

$$\Gamma_{nm,n'm'} = \int_0^{\pi} \mathcal{P}_n^m(\cos \theta) \mathcal{P}_{n'}^{m'}(\cos \theta) \qquad (1.134)$$

$$\times \left[ \delta_{m-m'} \cos^2 \theta + \frac{\sin[2(m-m')\eta_0]}{2(m-m')\eta_0} \sin^2 \theta \right] \sin \theta d\theta$$

In the absence of lateral interactions ($\varepsilon = 0$), each hypercolumn can exhibit orientation and spatial frequency tuning through spontaneous symmetry breaking of **SO**(3). This is a generalization of the **O**(2) symmetry breaking mechanism underlying orientation tuning in the ring model (see § 1.4). The orthogonality relation (1.119) shows that the eigenmodes are spherical harmonics with $\lambda = \lambda_n \equiv -1 + \mu W_n$ for $u(\theta, \varphi) = Y_n^m(\theta, \varphi)$, $-n \le m \le n$. Since $\lambda$ is $\mathbf{k}$-independent, the full solution for the eigenmodes can be written in the form

$$a(\mathbf{r}, \theta, \varphi) - a_0 = c_0(\mathbf{r}) Y_n^0(\theta, \varphi) + \sum_{m=1}^{n} \left[ c_m(\mathbf{r}) Y_n^m(\theta, \varphi) + \bar{c}_m(\mathbf{r}) \overline{Y_n^m}(\theta, \varphi) \right]$$

$$(1.135)$$

with the coefficients $c_m(\mathbf{r})$ arbitrary modulo the normalization condition

$$\sum_{m=0}^{n} |c_m(\mathbf{r})|^2 = B \qquad (1.136)$$

where $B$ is fixed. This normalization condition reflects the fact that the associated amplitude equations for the coefficients $c_m(\mathbf{r})$ are **SO**(3) equivariant [15].

Suppose that $W_1 > W_n$ for all $n \neq 1$. The fixed point $a = a_0$ then destabilizes at a critical value of the coupling $\mu_c = 1/W_1$ due to excitation of the first-order spherical harmonics. Sufficiently close to the bifurcation point, the resulting activity profile can be written as

$$a(\mathbf{r}, \theta, \varphi) = a_0 + c_0(\mathbf{r}) + \sum_{m=0,\pm} c_m(\mathbf{r}) f_m(\theta, \varphi) \qquad (1.137)$$

for real coefficients $c_0(\mathbf{r}), c_\pm(\mathbf{r})$ with $\sum_{m=0,\pm} c_m(\mathbf{r})^2 = B$ and

$$f_0(\theta, \varphi) = \cos\theta, \quad f_+(\theta, \varphi) = \sin\theta\cos\varphi, \quad f_-(\theta, \varphi) = \sin\theta\sin\varphi \quad (1.138)$$

Equation (1.137) represents a *tuning surface* for orientation and spatial frequency preferences for the hypercolumn at cortical position $\mathbf{r}$, which consists of a solitary peak whose location is determined by the values of the coefficients $(c_0(\mathbf{r}), c_+(\mathbf{r}), c_-(\mathbf{r}))$. Such a solution spontaneously breaks the underlying **SO**(3) symmetry. However, full spherical symmetry is recovered by noting that rotation of the solution corresponds to an orthogonal transformation of the coefficients $c_0, c_\pm$. Thus the action of **SO**(3) is to shift the location of the peak of the activity profile on the sphere, that is, to change the particular orientation and spatial frequency selected by the tuning surface. (This hidden **SO**(3) symmetry is explicitly broken by external stimuli, along similar lines to § 1.5.2).

The tuning surface generated by our spherical model has the important property that it is not separable with respect to orientation and spatial frequency – the activity profile cannot be written in the form $u(\theta, \varphi) = \Theta(\theta)\Phi(\varphi)$. Consequently, selectivity for orientation varies with spatial frequency. If $c_\pm = 0$ then the activity profile is peaked at the pinwheel associated with high $(c_0 > 0)$ or low $(c_0 < 0)$ spatial frequencies, and there is no selection for orientation. On the other hand, if $c_0 = 0$ then the activity profile is peaked at intermediate spatial frequencies and there is strong selection for orientation. It is important to emphasize that the tuning surface represents the activity profile of a population of cells within a hypercolumn, rather than the tuning properties of an individual cell. Thus the absence of orientation selectivity at pinwheels is an aggregate property of the population. Indeed, it has been found experimentally that individual cells around pinwheels are orientation selective, but there is a broad

distribution of orientation preferences within the pinwheel region so that the average response of the population is not orientation selective.

In order to solve the eigenvalue equation (1.130) for non-zero $\varepsilon$, we exploit the experimental observation that the lateral connections are weak relative to the local connections, and carry out a perturbation expansion in the small parameter $\varepsilon$. We show that there is a $q$–dependent *splitting* of the degenerate eigenvalue $\lambda_1$ that also separates out the first-order spherical harmonics. Denoting the characteristic size of such a splitting by $\delta\lambda = \mathcal{O}(\varepsilon)$, we impose the condition that $\delta\lambda \ll \mu\Delta W$, where $\Delta W = \min\{W_1 - W_m, m \neq 1\}$. This ensures that the perturbation does not excite states associated with other eigenvalues of the unperturbed problem, and we can then restrict ourselves to calculating perturbative corrections to the degenerate eigenvalue $\lambda_1$ and its associated eigenfunctions. Thus, introduce the perturbation expansions

$$\lambda = -1 + \mu W_1 + \varepsilon\lambda^{(1)} + \varepsilon^2\lambda^{(2)} + \ldots \tag{1.139}$$

$$A_{nm} = c_m\delta_{n,1} + \varepsilon A_{nm}^{(1)} + \varepsilon^2 A_{nm}^{(2)} + \ldots \tag{1.140}$$

and substitute these into the eigenvalue equation (1.130). We then systematically solve the resulting hierarchy of equations to successive orders in $\varepsilon$, taking into account the fact that the unperturbed problem is degenerate. Here we will only describe the lowest order corrections.

Setting $n = 1$ in equation (1.130) yields the **O**($\varepsilon$) equations

$$\sum_{m,m'=-1}^{1} \widehat{J}_{mm'}(q)c_{m'} = \lambda^{(1)}c_m$$

where $\widehat{J}_{mm'}(q) = J_{1m,1m'}(q)$. Using equations (1.126), (1.132) and (1.134), we find that

$$\begin{pmatrix} G_0(q) & 0 & 0 \\ 0 & G_0(q) & 4\chi G_2(q)/5 \\ 0 & 4\chi G_2(q)/5 & G_0(q) \end{pmatrix} \begin{pmatrix} c_0 \\ c_1 \\ c_{-1} \end{pmatrix} = \lambda^{(1)} \begin{pmatrix} c_0 \\ c_1 \\ c_{-1} \end{pmatrix} \tag{1.141}$$

where $\chi$ is given by equation (1.69). Equation (1.141) has solutions of the form

$$\lambda^{(1)} = \lambda_0^{(1)}(q) \equiv G_0(q) \tag{1.142}$$

with eigenmode $c_0 = 1, c_\pm = 0$ and

$$\lambda^{(1)} = \lambda_\pm^{(1)}(q) \equiv G_0(q) \pm \frac{4}{5}\chi G_2(q) \tag{1.143}$$

with eigenmodes $c_0 = 0, c_{-1} = \pm c_1$.

As a concrete example, suppose that $g(s)$ is given by equation (1.74) and $\chi = \sin 4\eta_0/4\eta_0$. Plotting $G_m(q)$ for $m = 0, 2$ establishes that when there is sufficiently strong anisotropy in the linear zones ($\eta_0 < \pi/4$)

$$\min_q\{\lambda_-^{(1)}(q)\} < \min_q\{\lambda_0^{(1)}(q)\} < \min_q\{\lambda_+^{(1)}(q)\} \tag{1.144}$$

and the marginally stables modes are of the form

$$a(\mathbf{r}, \theta, \varphi) = \sum_i b_i e^{i\mathbf{k}_i \cdot \mathbf{r}} \sin\theta \sin(\varphi - \zeta_i) \tag{1.145}$$

where $\mathbf{k}_i = q_c(\cos\zeta_i, \sin\zeta_i)$ and $q_c$ is the wavenumber that minimizes $\lambda_-^{(1)}(q)$. On the other hand, when there is weaker anisotropy within the linear zones ($\eta_0 > \pi/4$)

$$\min_q\{\lambda_+^{(1)}(q)\} < \min_q\{\lambda_0^{(1)}(q)\} < \min_q\{\lambda_-^{(1)}(q)\} \tag{1.146}$$

and the marginally stables modes are now of the form

$$a(\mathbf{r}, \theta, \varphi) = \sum_i b_i e^{i\mathbf{k}_i \cdot \mathbf{r}} \sin\theta \cos(\varphi - \zeta_i) \tag{1.147}$$

In both cases, these are states in which each hypercolumn has a tuning surface that peaks at intermediate frequencies. This regime is the one relevant to contour formation, and thus we recover the basic contoured patterns presented in § 1.6.4.

## 1.8 Future directions

There are many directions in which this work can be expanded. For example, it is now clear that many different features are mapped onto the visual cortex and beyond in addition to retinal position, orientation and spatial frequency. Thus ocularity, directional motion, binocular disparity, and colour seem to be mapped [39, 35, 6, 48, 36]. It therefore remains to work out the symmetry groups associated with these features and thence to apply the mathematical machinery we have introduced above to compute the patterns which arise via spontaneous symmetry breaking.

There is also the fact that the neuron model used to formulate equations (1.4) is extremely simplified. It is nothing more than a low–pass RC filter followed by a sigmoidal current–voltage characteristic. One can easily make this model more complex and realistic by adding recovery variables in the style of the Fitzhugh–Nagumo equations [64], or one can simplify it still further by using the well–known *integrate–and–fire* model [10]. Interestingly, in either case the dynamics is richer, and a variety of oscillatory phenomena are immediately apparent.

However the most interesting new direction is to study, not spontaneous but *driven* pattern formation in neural networks of the type we have introduced. This amounts to studying the effects of external stimuli on such networks. In our case this means studying the effects of visual stimuli. Depending on the order of magnitude of such stimuli, various effects are possible. Thus external stimuli of order $O(1)$ couple to the fixed points of equation (1.4), stimuli of order $O(\epsilon^{1/2})$ couple to the linearized equations (1.6), and $O(\epsilon^{3/2})$ stimuli couple directly to amplitude equations such as those of equation (1.52) and effectively unfold any bifurcation [10, 13]. The various effects produced by these and related stimuli remain to be studied in detail.

## 1.9   References

[1] Angelucci A, Levitt J B, Hupe J M, Walton E J S , Bullier J and Lund J S, 2000. Anatomical circuits for local and global integration of visual information: Intrinsic and feedback connections. *Europ. J. Neurosci.* **12** 285.

[2] Angelucci A, Levitt J B and Lund J S, 2002. Anatomical origins of the classical receptive field and modulatory surround field of single neurons in macaque visual cortical area v1. *Progress in Brain Research (in press).*

[3] Ben-Yishai R, Lev Bar-Or R and Sompolinsky H, 1995 Theory of orientation tuning in visual cortex. *Proc. Nat. Acad. Sci.* **92** 3844-3848

[4] Ben-Yishai R, Hansel D and Sompolinsky H, 1997 Traveling waves and the processing of weakly tuned inputs in a cortical network module. *J. Comput. Neurosci.* **4** 57-77

[5] Blasdel G G and Salama G, 1986 Voltage-sensitive dyes reveal a modular organization in monkey striate cortex. *Nature 321* 579-585

[6] Blasdel G G, 1992 Orientation selectivity, preference, and continuity in monkey striate cortex. *J. Neurosci.* **12** 3139-3161

[7] Bonhoeffer T, Kim D S, Malonek D, Shoham D and Grinvald A, 1995 Optical imaging of the layout of functional domains in area 17/18 border in cat visual cortex. *European J. Neurosci.* **7** 1973-1988

[8] Bosch Vivancos I, Chossat P and Melbourne I, 1995 New planforms in systems of partial differential equations with Euclidean symmetry. *Arch. Rat. Mech.* **131**: 199–224.

[9] Bosking W H, Zhang Y, Schofield B and Fitzpatrick D, 1997 Orientation selectivity and the arrangement of horizontal connections in tree shrew striate cortex. *J. Neurosci.* **17** 2112-2127.

[10] Bressloff P C, Bressloff N W and Cowan J D, 2000 Dynamical mechanism for sharp orientation tuning in an integrate–and–fire model of a cortical hypercolumn. *Neural Comput.* **12** 2473-2511

[11] Bressloff P C, Cowan J D, Golubitsky M, Thomas P J and Wiener M, 2001 Geometric visual hallucinations, Euclidean symmetry and the functional architecture of striate cortex. *Phil. Trans. Roy. Soc. Lond. B* **356** 299-330

[12] Bressloff P C, Cowan J D, Golubitsky M and Thomas P J, 2001 Scalar and

pseudoscalar bifurcations: pattern formation on the visual cortex. *Nonlinearity* **14** 739-775.

[13] Bressloff P C and Cowan J D, 2002 An Amplitude Equation approach to Contextual Effects in Visual Cortex. *Neural Comput.* **14** 493-525

[14] Bressloff P C, Cowan J D, Golubitsky M, Thomas P J and Wiener M, 2002 What geometric visual hallucinations tell us about the visual cortex. *Neural Comput.* **14** 473-491

[15] Bressloff P C and Cowan J D, 2002 **SO**(3) symmetry breaking mechanism for orientation and spatial frequency tuning in visual cortex *Phys. Rev. Lett.* **88** 078102

[16] Bullier J, Hupe′ J-M, James A J and Girard P, 2001 The role of feedback connections in shaping the response of visual cortical neurons. *Prog. Brain Res.* **134** 193-204.

[17] Clottes J and Lewis-Williams D, 1998 *The Shamans of Prehistory: Trance and Magic in the Painted Caves*. New York: Abrams.

[18] Cowan J D, 1997 Neurodynamics and Brain Mechanisms. In Ito M, Miyashita Y and Rolls E T, editors, *Cognition, Computation, and Consciousness* (Oxford University Press) p. 205-233

[19] Das A and Gilbert C, 1999 Topography of contextual modulations mediated by short–range interactions in primary visual cortex *Nature* **399** 655-661

[20] Dionne B, Golubitsky M, Silber M and Stewart I, 1995 Time–periodic spatially periodic planforms in Euclidean equivariant partial differential eqnarrays. *Phil. Trans. Roy. Soc. Lond. A* **325** 125-168

[21] Douglas R, Koch C, Mahowald M, Martin K and Suarez H, 1995 Recurrent excitation in neocortical circuits. *Science* **269** 981-985

[22] Ermentrout G B and Cowan J D, 1979 A mathematical theory of visual hallucination patterns. *Biol. Cybernetics* **34** 137-150

[23] Ermentrout G B, 1998 Neural networks as spatial pattern forming systems. *Rep. Prog. Phys.* **61** 353-430

[24] Fitzpatrick D, 2000 Seeing beyond the receptive field in primary visual cortex. *Curr. Op. in Neurobiol.* **10** 438-443

[25] Ferster D, Chung S and Wheat H, 1997 Orientation selectivity of thalamic input to simple cells of cat visual cortex. *Nature* **380** 249-281

[26] Gilbert C D and Wiesel T N, 1983 Clustered intrinsic connections in cat visual cortex. *J. Neurosci.* **3** 1116-1133

[27] Gilbert C D, 1992 Horizontal integration and cortical dynamics *Neuron* **9** 1-13

[28] Gilbert C D, Das A, Ito M, Kapadia M and Westheimer G, 1996 Spatial integration and cortical dynamics. *Proc. Nat. Acad. Sci.* **93** 615-622

[29] Golubitsky M, Stewart I and Schaeffer D G, 1988 *Singularities and Groups in Bifurcation Theory II.* (Berlin: Springer–Verlag)

[30] Haüssler A and von der Malsburg C 1983 Development of Retinotopic Projections: An Analytical Treatment *J. Theoret. Neurobiol.* **2** 47-73

[31] Hirsch J D and Gilbert C D, 1991 Synaptic physiology of horizontal connections in the cat's visual cortex. *J. Physiol. Lond.* **160** 106-154

[32] Hubel D H and Wiesel T N, 1962 Receptive fields, binocular interaction and functional architecture in the cat's visual cortex. *J. Neurosci.* **3** 1116-1133

[33] Hubel D H and Wiesel T N, 1974a Sequence regularity and geometry of

orientation columns in the monkey striate cortex. *J. Comp. Neurol.* **158** 267-294.

[34] Hubel D H and Wiesel T N, 1974 Uniformity of monkey striate cortex: A parallel relationship between field size, scatter, and magnification factor. *J. Comp. Neurol.* **158** 295-306.

[35] Hubel D H and Livingstone M S, 1987 Segregation of form, color, and stereopsis in primate area 18. *J. Neurosci.* **7** 3378-3415.

[36] Hubener M, Shoham D, Grinvald A and Bonhoeffer T, 1997 Spatial relationship among thre columnar systems. *J. Neurosci.* **15** 9270-9284.

[37] Issa N P, Trepel C and Stryker M P, 2000. Spatial frequency maps in cat visual cortex. *J. Neurosci.* **20** 8504-8514.

[38] LeVay S and Nelson S B 1991. Columnar organization of the visual cortex. *The neural basis of visual function* ed Leventhal A G (Boca Raton: CRC Press) pp 266-315

[39] Livingstone M S and Hubel D H, 1984 Anatomy and physiology of a color system in the primate visual cortex. *J. Neurosci.* **4** 309-356.

[40] Malach R, Amir Y, Harel M and Grinvald A, 1993 Relationship between intrinsic connections and functional architecture revealed by optical imaging and in vivo targeted biocytin injections in primate striate cortex. *Proc. Natl. Acad. Sci.* **90** 10469-10473

[41] Marr D and Poggio T, 1976 Cooperative computation of stereo disparity *Science* **194** 283-287

[42] Mundel T, Dimitrov A and Cowan J D, 1997 Visual cortex circuitry and orientation tuning. In Mozer M C, Jordan M I and Petsche T, editors, *Advances in Neural Information Processing Systems*, volume 9 (MIT Press) p. 886-893

[43] Obermayer K and Blasdel G G, 1993 Geometry of orientation and ocular dominance columns in monkey striate cortex. *J. Neurosci.* **13** 4114-4129

[44] Patterson A, 1992 *Rock Art Symbols of the Greater Southwest*. Boulder CO: Johnson Books.

[45] Phleger B and Bonds A B, 1995 Dynamic differentiation of gaba$_A$–sensitive influences on orientation selectivity of complex cells in the cat striate cortex. *Exp. Brain Res.* **104**

[46] Roberts M, Swift J and Wagner D H, 1986 The Hopf bifurcation on a hexagonal lattice. *Contemp. Math.* **56** 283-318

[47] Rockland K S and Lund J, 1983 Intrinsic laminar lattice connections in primate visual cortex. *J. Comp. Neurol.* **216** 303-318

[48] Shmuel A and Grinvald A, 1996 Functional Organization for Direction of Motion and its Relationship to Orientation Maps in Cat Area 18. *J. Neurosci.* **16** 6945-6964

[49] Shmuel A, Korman M, Harel M, Grinvald A and Malach R, 1998 Relationship of feedback connections from area V2 to orientation domains in area V1 of the primate. *Soc Neurosci. Abstr.* **24** 767

[50] Siegel R K and Jarvik M E, 1975 Drug-induced hallucinations in animals and man. In Siegel R K and West L J, editors, *Hallucinations: Behavior, Experience and Theory*, (New York: Wiley) p. 81-161

[51] Silber M and Knobloch E 1991 Hopf bifurcation on a square lattice. *Nonlinearity* **4** 1063-1107

[52] Somers D C, Nelson S and Sur M, 1995 An Emergent Model of Orientation Selectivity in Cat Visual Cortical Simple Cells. *J. Neurosci.* **15** 5448-5465

[53] Swindale N V, 1980 A model for the formation of ocular dominance stripes. *Proc. Roy. Soc. Lond. B* **208** 243-264

[54] Swindale N V, 1982 A model for the formation of orientation columns *Proc. Roy. Soc. Lond. B* **215** 211-230

[55] Swindale N V, 1996 The development of topography in visual cortex: a review of models *Network* **7** 161-247

[56] Tass P, 1997 Oscillatory cortical activity during visual hallucinations. *J. Biol. Phys.* **23** 21-66

[57] Toth L J, Rao S C, Kim D-S, Somers D C and Sur M, 1996 Subthreshold facilitation and suppression in primary visual cortex revealed by intrinsic signal imaging. *Proc. Natl. Acad. Sci.* **93** 9869-9874

[58] Turing A M, 1952 The Chemical Basis of Morphogenesis *Phil. Trans. Roy Soc. Lond. B* **237** 32-72

[59] Vidyasagar T R, Pei X and Volgushev M, 1996 Multiple mechanisms underlying the orientation selectivity of visual cortical neurons. *Trends in Neurosci.* **19** 272-277

[60] von der Malsburg C, 1973 Self-organization of Orientation Selective cells in the Striate Cortex. *Kybernetik* **14** 85-100

[61] von der Malsburg C and Willshaw D J, 1977 How to label nerve cells so that they can interconnect in an ordered fashion. *Proc.Natl.Acad.Sci. USA* **74** 5176-5178

[62] von der Malsburg C and Cowan J D, 1982 Outline of a Theory for the Ontogenesis of Iso–Orientation Domains in Visual Cortex. *Biol. Cybern.* **45** 49-56

[63] Willshaw D J and von der Malsburg C, 1979 A marker induction mechanism for the establishment of ordered neural mappings: its application to the retinotectal problem. *Philos. Trans. R. Soc. London, B* **287** 203-243

[64] Wilson H R and Cowan J D, 1972 Excitatory and inhibitory interactions in localized populations of model neurons. *Biophys. J.* **12** 1-24

[65] Wilson H R and Cowan J D, 1973 A mathematical theory of the functional dynamics of cortical and thalamic nervous tissue. *Kybernetik* **13** 55-80

[66] Yoshioka T, Blasdel G G, Levitt J B and Lund J S, 1996 Relation between patterns of intrinsic lateral connectivity, ocular dominance, and cytochrome oxidase–reactive regions in macaque monkey striate cortex. *Cerebral Cortex* **6** 297-310

[67] Zweck J W and Williams L R Euclidean group invariant computation of stochastic completion fields using shiftable-twistable functions. Submitted for publication 2001